

1 **TITLE: Capturing geological uncertainty in salt cavern developments for**
2 **hydrogen storage: Case study from Southern North Sea.**

- 3 i. Hector George Barnett*¹, Mark T. Ireland¹, Cees Van der Land¹
4 ii. ¹ Earth Ocean and Planetary Science Group, School of Natural and Environmental
5 Sciences, Drummond Building, Newcastle University, Newcastle Upon-Tyne NE1
6 7RU
7 iii. *Corresponding Author Email Address: h.barnett2@ncl.ac.uk

8 Keywords: Hydrogen Storage, Salt Caverns, Geological modeling, Energy Systems, Renewable
9 Energy

10
11 **PREPRINT STATEMENT**

12 This manuscript has not been peer-reviewed, it has been submitted to EarthArXiv
13 as a preprint. A subsequent version of this manuscript may have slight edits and
14 changes present. This manuscript has been submitted for publication in Earth
15 Science, Systems and Society. If accepted, the final version of this manuscript will
16 be available via the 'Peer-reviewed Publication DOI' link on the right-hand side of
17 this webpage.
18

19 **Abstract**

20 Future energy systems with greater contributions from renewable energy will require long-
21 duration energy storage to optimise integration of renewable sources, hydrogen is an energy
22 vector that could be utilised for this. Grid-scale underground natural gas storage is already in
23 operation in solution-mined salt caverns, where individual cavern capacities are ~25 - 275
24 GWh. While traditionally salt caverns have been restricted to being developed onshore, in
25 some offshore locations, such as the UK Continental Shelf, there are extensive evaporites that
26 have potential for storage development. Capacity estimates for offshore areas, typically rely
27 upon generalised regional geological interpretations, frequently do not incorporate site-
28 specific structural and lithological heterogeneities, use static cavern geometries, and use
29 methodologies that are deterministic and not repeatable.

30 We developed a stochastic method for identifying viable salt cavern locations and estimating
31 conceptual clusters' storage capacity. The workflow incorporates principle geomechanical
32 constraints on cavern development, captures limitations from internal evaporite
33 heterogeneities, and uses the ideal gas law to calculate the volumetric capacity. The workflow
34 accommodates either fixed cavern geometries or geometries that vary per site depending on
35 the thickness of salt. By using a stochastic method, we quantify uncertainties for storage
36 capacity estimates and cavern placement across defined regions of interest. The workflow is
37 easily adaptable allowing users to consider multiple geological models or evaluate the impact
38 of interpretations of varying resolutions.

39 We illustrate the workflow for four areas and geological models in the UK's Southern North
40 Sea:

- 41 1) Basin Scale (58,900 km²) - >61.9 PWh's of hydrogen storage with >199,000 cavern
42 locations.
- 43 2) Sub-Regional Scale (24,800 km²) – >12.1 PWh's of hydrogen storage with >36,000
44 cavern locations.
- 45 3) Block Specific – Salt Wall (79.8km²) - >731 TWh's of hydrogen storage with >400
46 cavern locations.
- 47 4) Block Specific – Layered Evaporite (225 km²) - >419 TWh's of hydrogen storage with
48 >460 cavern locations.

49 Our workflow enables reproducible and replicable assessments of site screening and storage
50 capacity estimates. A workflow built around these ideals allows for fully transparent results.
51 We compare our results against other similar studies in literature and find that often highly
52 cited papers have inappropriate methodologies and hence capacities.

53

54 **1. Introduction**

55 Long-duration energy storage (LDES) will be a vital feature in future energy systems
56 (McNamara et al., 2022; Smdani et al., 2022). As renewable and low-carbon energy displaces
57 fossil fuels there will be a requirement to accommodate the increased variability in supply
58 that comes with this transition (Dowling et al., 2020). LDES allows for the management of grid
59 imbalances that arise from both the variable supply of renewable energy and the variability
60 on the demand side, while improving the overall flexibility and reliability of the energy system
61 (Kueppers et al., 2021; Sepulveda et al., 2021). There are three principal mechanisms for
62 geological LDES: mechanical (compressed air or solid weight), thermal, and chemical energy
63 storage (hydrogen, ammonia, natural gas) (Bauer et al., 2013; Shan et al., 2022). Chemical
64 storage is often considered the most versatile option of these three, as the energy storage
65 medium can also be transported and used with relative ease and with a low energy loss
66 (<0.1% vs 5% for high voltage energy cables), over long distances, adding to the flexibility of
67 the energy system as a whole (Calado and Castro, 2021).

68 Subsurface formations have proven to be suitable storage containers for geological scales of
69 time, as evidenced by the occurrence of natural hydrocarbon accumulations (Lokhorst and
70 Wildenborg, 2006). The subsurface has already been utilized for many decades for the storage
71 of natural gas. The Rough gas storage field, for example, located offshore UK, has been in
72 operation since 1985 (with a 5-year hiatus from 2017 - 2022) with the capacity to store 54
73 BCF of natural gas (Centrica, 2023), or in Cheshire, UK, Storengy operates a salt cavern cluster
74 consisting of 28 caverns with the ability to store 14 BCF of gas (Eising et al., 2021). Hydrogen
75 has also been stored within the subsurface, the Spindletop salt caverns cluster in Texas, USA,
76 for example, which stored 5 BCF (≈ 1450 GWh) of natural gas, was converted to store 274
77 GWh of hydrogen (Bérest et al., 2021). Compared with other methods of LDES, such as Li-Po
78 batteries and pumped-hydro, subsurface geological storage provides several advantages,
79 such as, greater capacities, small surface footprint, low specific investments and operating
80 costs, operational timespans for over 30 years, and increased security (Crotogino et al., 2017).
81 There are two differing storage methods within the subsurface, porous media (e.g. saline
82 aquifers and abandoned hydrocarbon fields) or salt caverns (Bauer et al., 2013; Evans, 2007).
83 Salt caverns for hydrogen storage are the technology of investigation within this study, as,
84 while research has been undertaken on hydrogen storage in porous media such as
85 Heinemann et al. (2018), Heinemann et al. (2021) and Hassanpouryouzband et al. (2022),

86 storage of hydrogen in porous media has yet to be deployed, whereas there are several salt
87 cavern clusters storing hydrogen currently in operation.

88 Salt caverns are solution mined voids within a evaporitic (salt) layers (Tarkowski and
89 Czapowski, 2018; Warren, 2006). They range volumetrically from 70,000 m³ (e.g Teesside, UK
90 (HyUnder, 2013)) to 17,000,000 m³ (Texas (Leith, 2000)). Salt caverns are an established
91 technology having been in use since 1960's for storing gas (Allen, 1972). Hydrogen has been
92 stored within salt caverns since the early 1970's for use in chemical industry, with the first
93 site located in Teesside, UK (Caglayan et al., 2020; François, 2021; Landinger and Crotofino,
94 2007) and other select locations elsewhere in the world. Recent published work on salt cavern
95 volumetrics has focused on onshore areas, and frequently at a country-wide scale analysis for
96 capacity estimates and cavern placement (e.g. Caglayan et al. (2020) and Williams et al.
97 (2022)), modelled capacity estimates across whole basins greatly exceed the estimated
98 requirements for LDES. The estimates make use of coarse-resolution geological models and
99 are not able to capture the geological complexity of both the salt layers, and the overlying
100 geological complexity. Simplified, or basic geological models may not reliably estimate cavern
101 placement options, and their storage capacity. In the UK to date, there has not been a
102 systematic assessment of the geological constraints on offshore salt cavern development.
103 However, offshore salt caverns are not outside technological feasibility (Costa et al., 2017).
104 One of the possible benefits from offshore storage is the co-location of storage next to
105 offshore windfarms, or pre-existing pipelines, developing both a hub of energy production
106 and storage. Salt caverns are typically developed in clusters (Gillhaus., 2007) and the work
107 here could be considered as the basis for pre-feasibility studies of cavern placement options.

108 We demonstrate the robustness and flexibility of our methodology for the offshore of the UK.
109 The UK is currently undergoing a shift in the supply of energy to meet its 2050 net-zero
110 obligations, with installed wind power capacity in 2023 reaching 27.9 GW (Staffell et al.,
111 2023). For 100% renewable penetration by 2035 in the UK, Cárdenas et al. (2021) found that
112 with the optimum mix of renewable technologies and allowing for over-generation, the UK
113 would require ~42 TWh of LDES, far lower than the suggested 115 TWh needed if no over
114 generation is allowed. The UK's Electricity System Operator (2023) states that a whole energy
115 system transformation by 2050 would require the UK to have 56 TWh of hydrogen storage by
116 2050. Without the utilisation of LDES within the energy mix it will be difficult for the UK to
117 achieve its legislated net-zero carbon goals (King et al., 2021). Geological storage is currently
118 the most viable option for LDES within the UK as: 1) there are a number of possible location
119 options distributed across the UK, and the location of storage is an important consideration
120 in the whole system (Sunny et al., 2020); 2) pre-existing oil and gas infrastructure could be
121 repurposed to reduce capital expenditure associated with LDES scale up (Oil and Gas
122 Authority, 2021); 3) Geological storage is estimated to currently be one of the lowest cost
123 LDES options available (Hunter et al., 2021).

124 We focus on the Southern North Sea area of the UKCS due to the data availability, geological
125 suitability, and possible future demand for hydrogen storage within the area. Four areas of
126 interest (Aols) are defined within our study (Figure. 1) to consider the potential locations and
127 capacity for salt caverns for hydrogen storage within Zechstein supergroup. The Zechstein
128 supergroup is a Late Permian-aged layered evaporite sequence deposited during the
129 Lopingian (Peryt et al., 2010), it is laterally extensive, and, across large areas exceeds 750 m
130 in thickness. It is located within both the North Permian and South Permian Basins of Europe,
131 where it extends from onshore the eastern coast of the UK, across to western Poland

132 (Glennie, 1998). The Zechstein Supergroup is found as both layered and structured salt
133 throughout both basins, with most of the current understanding coming from hydrocarbon
134 exploration and development, where it is important for trapping mechanisms and sealing
135 reservoir intervals (Doornenbal et al., 2019; Glennie, 1998; Grant et al., 2019; Strozyk, 2017).
136 The Zechstein's deposition as a layered evaporite sequence is typically divided into five cycles,
137 however the nomenclature used frequently varies depending on regional location and
138 environment of deposition (Johnson et al., 1993). The internal heterogeneity of the Zechstein
139 varies in complexity across the Southern North Sea due to the Zechstein's mobility from
140 halokinesis (Barnett et al., 2023).

141

142 **2. Methodology**

143

144 **2.1 Workflow**

145 The workflow in this study uses a geological model as the input and determines an idealised
146 cavern layout and calculates the resulting working hydrogen storage capacity (Appendix. 1).
147 Due to the inherent uncertainty associated with geological models, the method
148 accommodates both deterministic and stochastic inputs. The workflow is agnostic to the
149 resolution of the input geological models, recognising that the availability of data varies by
150 area. The method can incorporate stochastic inputs in which case the workflow is run as a
151 Monte Carlo simulation, capturing the inherent uncertainty of the geological model. The
152 workflow is a robust and repeatable method to determine the placement of salt caverns and
153 calculate the hydrogen storage capacity. The workflow can be set to optimise for either
154 cavern number or capacity, allowing for idealised utilisation of the area of interest.

155 The workflow initially removes areas of the geological model that have been determined as
156 unsuitable based on the set parameters (Appendix. 1). The suitability of these areas for cavern
157 placement is treated as binary condition, either suitable or not. It is possible to incorporate
158 surface constraints, such as roads or population areas in onshore areas, or energy
159 infrastructure offshore. Buffers can be applied to these features, which then determine a set
160 distance for caverns to be placed.

161 The depth to geological formations can be constrained using seismic and well data, where
162 seismic is used to interpret between the depth calibrated measurements from wells. As a
163 result, depths in geological models have an inherent level of uncertainty. We accounted for
164 this by using a uniform distribution calculated from the residual depth values calculated
165 during the depth conversion process. The largest residual value from the depth conversion
166 process was calculated as a percentage and set both the positive and negative limits of the
167 uniform distribution. As depth uncertainty can be either positive or negative, setting the
168 maximum residual to limit the uniform distribution (E.g., -10% and +10%) allows the workflow
169 to account for depth uncertainty.

170 The workflow assumes that every grid cell within the geological model which has not been
171 removed is a viable location for cavern placement. The height-to-diameter ratio at each viable
172 location is determined by using the salt thickness at that location (Appendix. 1 - Equation. 1).
173 From the salt thickness and height-to-cavern ratio, a cavern geometry is determined
174 (Appendix. 1 - Equations 2 - 6). If a fixed cavern geometry is used, then the pre-set maximum

175 cavern height and cavern diameters are used instead. The shallowest a cavern can be
176 emplaced in salt is 500 m (Caglayan et al., 2020; Tan et al., 2021; Warren, 2006), if a possible
177 cavern location is in very shallow salt <500 m, it is checked to see if the salt is deeper than
178 500 m and has sufficient thickness beyond 500 m depth than the minimum cavern
179 geometrical requirements. If so, a viable cavern is placed at 500 m deep. This optimisation
180 allows for higher operating pressures, and hence higher hydrogen capacities in areas of
181 shallow but thick salt (Appendix. 1 - Equation. 12).

182 The minimum distance between cavern mid points (buffer distance, Figure. 2) is then
183 determined to establish the viable combination of adjacent cavern locations (Appendix. 1 -
184 Equation. 7) and is a simplified approach to account for the geomechanical requirements for
185 stability between adjacent caverns (Caglayan et al., 2020; Ma et al., 2022). Where the grid cell
186 spacing is greater than the buffer distance between caverns then there will be overlap
187 between buffers. To determine a layout where there is no overlap of buffers the workflow
188 iterates horizontally through the array of viable cavern locations starting at 0,0 (top left), plots
189 a cavern, checks to see if the buffer overlaps with another caverns' buffer, and if it does not,
190 keeps it, if it does, it is deemed unviable and removed. Further explanation of how this works
191 can be seen in the Appendix under 'cavern best fit algorithm'. This methodology optimally
192 packs the caverns within the areas viable for cavern placement.

193 The volume for each cavern is then calculated, (Appendix. 1 - Equation. 8). For caverns with a
194 height-to-diameter ratio of < 1, an ellipsoid shape was assumed for the volume (Appendix. 1
195 - Equation. 8b), as pill geometries become ellipsoids with a height-to-diameter of <1. The
196 volume for the cavern will depend on its planned geometrical shape. Our workflow uses pill
197 geometries for the 3D cavern shape (Figure. 2), as these are the most stable and have the
198 lowest stress risk (Ozarslan, 2012) (Appendix. 1 - Equation. 8).

199 Remaining are all viable cavern locations within the area with correct spacing and geometries
200 for the salt present. Lithostatic pressure for the mid cavern depth are calculated as they
201 determine the cavern operating pressure. A simple 1D layer cake approach can be taken for
202 calculating lithostatic pressure (Appendix. 1 - Equation. 9) depending on data available
203 (Section 2.2.3). For layer cake models, the same depth uncertainty is applied to that of the
204 salt depth and thickness surfaces. An uncertainty can also be applied to the density of the
205 overburden layers. Internal cavern temperatures are then calculated from a set geothermal
206 gradient (Appendix. 1 - Equation. 10, Section 2.2.2). The cavern volume is then adjusted to
207 account for the insoluble content that is present within the salt (Appendix. 1 - Equation. 11,
208 Section 2.2.1), a simple % may be used or a distribution derived from well data.

209 Individual cavern hydrogen capacity is then calculated using the ideal gas law (Appendix. 1 -
210 Equation. 12). 60% of the lithostatic pressure at mid cavern depth is used to calculate the
211 working capacity as a cushion gas of 20% is required to maintain cavern integrity and a
212 maximum pressure inside caverns is set at 80% to avoid exceeding the fracture gradient
213 (Caglayan et al., 2020; Muhammed et al., 2022; Ozarslan, 2012). Once the individual capacity
214 of each cavern is known, the energy capacity for the whole area or a cavern cluster can be
215 calculated (Appendix. 1 - Equation. 13). The energy capacity calculations are modifiable to
216 allow for different energy vectors, such as natural gas, compressed air, or other gases.

217 From the Monte Carlo simulation, p10, p50 and p90 values can be calculated. The outputs
218 from this workflow allow not only for numerical capacity and cavern number but also the
219 geospatial data.

220 **2.2 Model Parameters**

221 **2.2.1 Insoluble Content**

222 Extensive data from across the UK sector of the Southern North Sea's South Permian Basin
223 was used for calculating the range of insoluble contents. The Z2 Stassfurt halite was the
224 chosen Zechstein salt layer for which to calculate insolubilities for as it is typically the thickest
225 salt unit within the South Permian Basis and the most likely to have cavern emplaced within
226 it. It was hence decided that the distribution to be used for insolubility content was that of
227 the Z2 Stassfurt halite from the whole of Southern North Sea basins (Appendix. 2 - 4).

228 Insoluble content was calculated from well logs as:

229 *Equation A:*
$$Ic = \frac{\Delta Z_{IC}}{\Delta Z_{TES}} * 100$$

230 $Ic =$ Insoluble content %

231 $\Delta Z_{IC} =$ Length insoluble lithology in target evaporite stratigraphy

232 $\Delta Z_{TES} =$ Total length of target evaporite stratigraphy

233

234

235 **2.2.2 Temperature**

236 Bottom hole temperatures were examined for all wells that had available data within the
237 South Permian Basin from the CGG Geothermal Database (see Data Availability). Geothermal
238 gradients were calculated from all the wells within the Basin Wide Area Aol (Figure. 1) within
239 the geothermal database. From these calculated gradients, minimum and maximum gradients
240 were extracted. The minimum maximum values set the bounds of a uniform distribution for
241 geothermal gradients to use in the calculation of mid-cavern temperature (Appendix. 1). The
242 geothermal gradient was then used in Equation B to calculate cavern temperature. A sea floor
243 temperature of 12 c° was assumed (Department for Environment Food and Rural Affairs,
244 2014).

245 *Equation B:*
$$T_{mc} = T_{sb} + (Z_{mc} * \nabla T)$$

246 $T_{mc} =$ Mid Cavern Temperature

247 $T_{sb} =$ Seabed temperature

248 $Z_{mc} =$ Mid Cavern depth below sea floor

249 $\nabla T =$ Geothermal gradient

250 **2.2.3 Overburden Pressure**

251 Two separate approaches for this were taken dependent on data available. 1) For areas where
252 data for the above layers of the overburden were available as well as density data, a layer
253 cake approach was used (Appendix. 1 - Equation. 9). Due to the geological surfaces being used
254 for thickness calculations and affected by the uncertainty in the depth conversion, these

255 values were modified to the same uncertainty distribution that had been applied to the
256 geological surfaces. Bulk density well logs were used to calculate the average densities for
257 each of the geological layers in Appendix. 1 - Equation 9. These values were also subject to a
258 certain level of uncertainty, so to account for this it was decided that a uniform distribution
259 of +/-10% was applied to the densities on each model run. This was not applied for the water
260 column layer, instead, a constant value of 1024 Kg/m³ was applied.

261 2) For areas where the data was not available to make a layer cake model, a simple 2-layer
262 depth/gradient approach was used which accounted for both the water column and rock
263 overburden separately. The gradient of the rock overburden was calculated from the average
264 overburden density, a value of 1024 kg/m³ assumed for the water column and the depth
265 taken from the cavern mid-point. (Appendix. 1 - Equation. 9b).

266 **2.3 Well and Seismic Data Interpretation Methodology**

267 **2.3.1 Well data interpretation.**

268 Petrophysical logs were interpreted to distinguish different lithologies and hence different
269 stratigraphic intervals. A combination of gamma-ray, sonic, and density logs were used
270 alongside the supplied site geological descriptions and cuttings from the wells. For each well
271 lithologies were interpreted. These applied well tops were quality controlled against the NSTA
272 well top database and onsite geological reports for the well. For the Zechstein supergroup
273 stratigraphy, however, lithologies were applied to the highest resolution allowed by the
274 petrophysical logging tools. This resolution varies depending on the type of logging tool used;
275 however, it typically ranges from 1 – 5 m (Bourke et al., 1989). Following this, well-tops were
276 applied for the intra Zechstein stratigraphy, using the same QC as used for the non-Zechstein
277 stratigraphy. This well interpretation allowed for the interpretation of the key geological
278 horizons within the seismic data.

279 **2.3.2 Seismic Well Tie**

280 Synthetic-seismic well ties were generated to correlate the interpreted stratigraphic
281 boundaries from the well data that was in the depth domain (m) to the seismic data that was
282 in the time domain (ms). Synthetic traces were generated using a 35hz ricker wavelet and
283 extracted wavelets. These were compared with the original seismic data and the best match
284 selected to be used. The wells were bulk shifted vertically to assure the most suitable time-
285 depth match between well and seismic data, the top Zechstein seismic reflection was aimed
286 to be matched by the bulk shifting process.

287 **2.3.4 Seismic Data Interpretation**

288 The reflections identified as key stratigraphic boundaries were then interpreted on the
289 seismic data. Reflections of stratigraphic boundaries were initially mapped at intervals of 25
290 m in both the crosslines and inlines of the seismic data. Once suitable coverage of the area
291 had been achieved, 3D auto tracking was used to complete the interpretation surface. If areas
292 were not mapped by the auto-tracking, they were manually remapped in smaller increments
293 and then re-autotracked. This process was repeated until suitable interpretations of each key
294 reflection had been achieved. From these reflection interpretation horizons, surfaces were
295 generated, the surfaces had a grid spacing of 50 x 50 m and used a convergent gridding
296 algorithm. This process produced seamless surfaces.

297 Geological faults were mapped within the seismic data. To accomplish this, the view of the
298 seismic data was set perpendicular to the direction of the fault plane, and the visible fault line

299 mapped. Intersection intervals of 25 m were used, with the view of the seismic data being re-
300 orientated if the fault orientation changed. Faults were mapped until they could not be
301 perceived anymore within the seismic data.

302 **2.3.5 Seismic Depth Conversion**

303 Depth conversion is required where seismic data are in the time domain since all calculations
304 used to determine cavern placement and geometry require depth as a constraint. To depth
305 convert we follow a standard approach of using geophysical logs to determine the velocity
306 structure in the subsurface. This is subsequently used to determine interval velocities for the
307 layers within the geological model. Time-depth relationship data was extracted from wells
308 within the area and generated time surfaces used at the identified velocity interval. The
309 model generally has residuals <10 %. For a complete description of the depth conversion
310 method please see the data repository.

311 **2.4 Sensitivity Analysis**

312 A sensitivity analysis was undertaken for two separate AOI's and geological models, the
313 layered evaporite block and the salt wall block (Section 4.3.1 and 4.3.2). A Sobol sensitivity
314 analysis used 1000 iterations and was implemented with the use of the SALib python module
315 (Herman and Usher, 2017; Iwanaga et al., 2022; Sobol', 2001). For the sensitivity analysis, four
316 parameters were included: depth uncertainty, geothermal gradient, insolubility, and
317 overburden gradient.

318 **3. Data and Interpretation**

319 **3.1 Basin Wide Salt Depth Model**

320 The basin wide depth model covers an area of 58,904 km² (Figure. 1). The surfaces used in
321 the model have a grid cell size of 250 m, the lowest resolution of depth models used. The
322 surfaces were from are from the 'NSTA and Lloyd's Register SNS Regional Geological Maps
323 (Open Source)' dataset and available from the NSTA public open data repository
324 (<https://opendata-nstauthority.hub.arcgis.com/explore>). No information was supplied
325 regarding depth uncertainty. We assume a 10% depth uncertainty.

326 **3.2 Sub Regional Salt Depth Model**

327 The depth surfaces for the sub regional salt depth model are from Barnett et al. (2023) and
328 cover 25,000 km² (Figure. 1). The surfaces are from the interpretation of a regionally extensive
329 3D seismic volume of the Southern North Sea (OA__2019seis0001a), with top and base
330 Zechstein surfaces having already been converted from the time to depth domain. The grid
331 cell size is 50 m. The depth surfaces have a 5% uncertainty associated with them.

332 **3.3 Block Specific**

333 Blocks, when referring to the offshore energy industry, define set areas in which licences have
334 been granted for specific activities, such as oil and gas exploration, or more recently, carbon
335 capture and storage. Gas storage licences are also awarded as blocks from the UK's North Sea
336 Transition Authority, with Centrica being awarded a licence for the Rough Gas storage site in
337 2022 (North Sea Transition Authority, 2022). Exploration blocks in the Southern North Sea are
338 on average 115 km², with the largest being 250 km². We aimed to mimic these spatial
339 constraints when applying our workflow, as it is likely that licences and areas for gas storage
340 in salt caverns will be granted in a similar manner by the North Sea Transition Authority.

341 **3.3.1 Salt Wall Salt Depth Model**

342 The depth surfaces from the salt wall cover an area of 420 km² (Figure. 1). It is located on a
343 structure often referred to as the Audrey salt wall (Elam, 2007), which trends NNW – SSW in
344 the UK sector of the South Permian Basin. The depth surfaces were extracted from the Sub
345 regional depth model, and thus the grid cell sizing of 50 m and depth uncertainty of 5% remain
346 the same.

347 **3.3.2 Layered Evaporite Salt Depth Model**

348 The layered evaporite salt depth model covered an area of 225 km² (Figure. 1). It is located at
349 the northern edges of the South Permian Basin, just south of the Mid-North Sea High (Figure.
350 1). Seismic survey MA933F0002 was used to interpret top and base target salt, and other
351 major stratigraphic reflections for the area (Appendix - Table. A). The reflection chosen as top
352 target salt was the top of the Stassfurt halite and base target salt was base Stassfurt halite
353 because the thickest and most homogenous section of halite was at this section in the
354 interpreted well data (Figure. 3, 4). Two-way time surfaces were created as described in
355 section 2.3.4. As the surfaces were in two-way time, they had to be depth converted. The
356 depth conversion model used 5 layers (All those in Appendix - Table. A, excluding base
357 Zechstein) and time-depth relationship data was taken from 2 wells within the area (See Data
358 Repository). Our depth conversion model ended up with an average residual of 7% at the top
359 of the target salt unit. Further information regarding the depth conversion process can be
360 seen in the Data Repository. The final depth surfaces had a grid cell size of 50 m, and a residual
361 uncertainty of 7%. Within the Stassfurt halite there were heterogeneities observed that were
362 interpreted to be none-halite (insoluble) lithologies. These heterogeneities were difficult to
363 interpret on seismic data due to the seismic reflections within the area abruptly terminating
364 and being noisy. The area in which these heterogeneities were observed was instead mapped
365 using seismic time slice views within the Stassfurt halite.

366 **3.4 Geological Model Setup**

367 Seven separate geological models were devised using the depth models in section 3.1 – 3.3
368 (Appendix - Table. B). The models were devised to investigate different scales, cavern design,
369 data quality and salt type on the effect on cavern placement. Parameters for the workflow,
370 such as minimum salt thickness and maximum depth were taken from literature and can be
371 found in Appendix - Table. C. Each geological model (Appendix - Table. B) was ran as a
372 montecarlo simulation for a total of 2500 iterations.

373

374 **4.0 Results**

375 **4.1 Basin Wide**

376 **4.1.1 Basin Wide – Fixed caverns**

377 The p50 cumulative storage capacity from the basin wide geological model contains is 61.9
378 PWh (Figure. 5). The p90 and p10 capacities are 49.4 and 80.9 PWh. For cavern number the
379 p50 value is 199,692, with a p90 and p10 of 163,789 and 255,467. The average cavern capacity
380 for the Montecarlo iteration closest to the p50 value (iteration 149) is 308.5 GWh. Iteration
381 149 of the Montecarlo (geospatial representative of the p50 capacity) can be seen in Figure
382 5. Individual cavern capacity falls towards the edges of the basin and placement in the basin
383 depocenter is typically restricted to salt structures (Figure. 5).

384

385 **4.2 Sub-Regional**

386 **4.2.1 Sub-Regional – Fixed caverns**

387 The p50 capacity of the sub-regional basin scale geological model is 12.1 PWh, the p90 and
388 p10 are 10.1 and 15.82 PWh's. The cavern number p50 is 36,331 viable cavern locations and
389 the p90 and p10 are 30,233 and 46,674 caverns respectively. Iteration 141 of the Montecarlo
390 simulation is the spatial representative of the p50 result is present in Figure. 6. The locations
391 identified for the development of caverns predominantly show that cavern placement in the
392 mid basin follows the orientation of the major salt structures. 29.7% of caverns of the p50
393 model are plotted in salt walls and diapirs, despite walls and diapirs only accounting for 5.6%
394 of the total area of the sub-regional basin area (1400 km²). The remaining 70.3 % of caverns
395 are plotted at the basin edges to the west to north towards the Mid-North sea high, where
396 the cavern placement is more uniformly located in layered evaporite area salt areas (Figure.
397 6).

398 **4.3 Block Specific**

399 **4.3.1 Salt Wall**

400 **4.3.1.1 Salt Wall - Variable Cavern**

401 The p50 capacity of the salt wall – variable cavern run is 731 TWh, p90 and p10 capacities are
402 709 and 752 respectively (Figure. 7A-B). We identify 409 caverns could be fit in the salt wall
403 (Figure 7A). Despite the stochastic approach applied to the salt surfaces to account for depth
404 uncertainty, the interpreted salt thickness which is typically greater than 2500 m means that
405 the 5% depth uncertainty does not affect how many caverns can be placed. All caverns had
406 the same geometries despite being set to variable in the workflow. This occurred as all
407 locations had greater thickness than the maximum allowable cavern height (750 m, Appendix
408 - Table. B-C) and hence had the same height-to-diameter ratio applied to them. This resulted
409 in all caverns volumes before being adjusted for insoluble content to be the same at 5,628,686
410 m³.

411 **4.3.1.2 Salt Wall - Fixed Cavern**

412 The p50 capacity of the salt wall geological model with caverns of fixed geometry (Appendix
413 - Table. B) was 225 TWh, the p90 and p10 results are 219 and 231 TWh (Figure. 7C-D). The
414 total number of viable cavern locations within the area ranges between 1154 and 1151,
415 depending on the depth uncertainty applied (Figure. 7C-D). Small edge case variations
416 between the Montecarlo iterations caused by the associated depth uncertainty %, cause small
417 areas to become viable and nonviable, causing the small change in cavern number, similar to
418 that of the salt wall variable cavern number.

419 **4.3.2 Layered Evaporite**

420 **4.3.2.1 Layered Evaporite - Variable Cavern**

421 The p50 capacity of the layered evaporite – variable caverns geological model is 419.2 TWh,
422 p90 and p10 are 387.5 and 449.5 TWh. The p50 for cavern number is 448 viable cavern
423 locations (Figure. 8, Table. 1) with 358 and 501 for the p90 and p10 cavern locations
424 respectively (Figure. 8, Table. 1). Table 1 has the closest model iterations output to the p10,
425 p50 and p90 capacity values (Figure 8). The iteration closest to the p50 has the smallest
426 number of caverns present (as our workflow optimises for individual capacity), however it has
427 the largest working average cavern working capacity with 2330 GWh compared with 2079
428 GWh of the p90 and 2004 GWh of the p10. Whilst the model closest to the p10 has the lowest
429 average working capacity per cavern, it has the greatest total working capacity, this is due to

430 the increased number of caverns present in this model iteration compared with the other
431 models. The iterations closest to the p50 and p90 have a similar number of caverns placed,
432 however the p50's greater average working capacity gives the model greater total working
433 capacity.

434

435 **4.3.2.2 Layered Evaporite - Fixed Cavern**

436 The p50 capacity of the layered evaporite – fixed caverns geological model is 260.3 TWh,
437 158.9 TWh less than that of the variable cavern model for same AoI (Figure. 9). The p90 and
438 p10 capacity values are 184.8 and 277.6 TWh respectively. The p50 for cavern placement is
439 832, p90 and p10 for cavern number are 606 and 861 viable locations. The iteration from the
440 Montecarlo simulation with the closet hydrogen value to the p50 capacity has a total of 839
441 viable cavern locations, 372 more caverns than the equivalent variable cavern p50 iteration.
442 The fixed caverns however have a much lower average capacity, with value of 310 GWh,
443 compared with 1990 GWh of the variable caverns.

444 **4.3.2.3 Layered Evaporite - Basin Wide Depth Model – Variable Cavern**

445 The p50 capacity of the layered evaporite – basin wide depth model - variable caverns was
446 798.7 TWh (Figure. 10), the p90 and p10 capacities are 727.1 and 889.5 TWh. The p50 for
447 cavern placement is 495, p90 and p10 for cavern number are 479 and 503 viable locations.
448 The resultant geospatial distribution of the caverns differs from the site-specific depth model
449 (4.4.1), as there are large gaps between placed caverns (Figure. 10). The caverns placed have
450 a higher average capacity than the site-specific geological model (Section 4.4.1) 1616.7 GWh
451 vs 897.6 (closest iteration to the p50 capacity of both models).

452

453 **4.4 Conceptual cavern cluster developments**

454 While cumulative hydrogen capacity across large tracts of basins may be useful for initial
455 comparison of storage potential, a more useful consideration is the capacity of a salt cavern
456 cluster development. We therefore consider five conceptual salt cavern cluster developments
457 as a demonstration of how the workflow could aid in early-stage planning for a possible
458 cavern site at the project pre-feasibility stage (Figure. 11). The theoretical cluster concepts
459 were developed using iteration 175 (Figure. 8) from the Montecarlo simulation, the iteration
460 where the sum hydrogen capacity was closest to the p50 of the block specific – layered
461 evaporite – variable cavern model (Section 4.4.1). We assume three different development
462 scenarios 1) Maximum hydrogen storage capacity within a 1.5 km radius of fixed point; 2)
463 Maximum hydrogen storage capacity within a 3 km cluster radius of fixed point; 3) Maximum
464 cavern number within a 1.5 km radius of fixed point; 4) Maximum cavern number within a
465 3km radius of fixed point; 5) Storage capacity within 1.5 km radius of pre-existing
466 infrastructure (wellbore 41/05-1) (Figure. 1,4). Radiuses of 1.5 – 3 km are considered viable
467 step-out or deviation distances from a central facility point for development of individual
468 caverns. The geographic layout of the development concepts is shown in Figure. 11, and a
469 summary of results is in Table. 2.

470 **4.5 Sensitivity Analysis**

471 The sensitivity analysis for the layered evaporite and salt wall cavern sites (4.3.1.1 and 4.3.2.1)
472 (Figure. 12, A, B, Appendix - Table. D) shows both sites are most sensitive to insolubility
473 content and overburden gradient. Both sites are about equally as sensitive to geothermal

474 gradient as one another, however a key difference is with the sensitivity to depth uncertainty.
475 The salt wall model is not sensitive to changes in depth uncertainty, while the layered
476 evaporite model is. Depth uncertainty was 7% for the layered evaporite model and 5% for the
477 salt wall model, however within these areas, the depth uncertainty modified the depth
478 surfaces for the layered evaporite model, such that areas for cavern emplacement were no
479 longer viable, for the salt wall which is both shallow and very thick, the 5% modification to
480 depth surfaces did not make any areas unviable and hence the salt wall is not sensitive to
481 depth uncertainty.

482 **5. Discussion**

483 **5.1 Capacities and volumetrics and cavern placement**

484 The results described demonstrate the value in stochastic approaches to evaluating geological
485 energy storage. The case studies demonstrate the importance of high-veracity geological
486 models as inputs for such analysis. The results presented indicate that theoretically salt
487 cavern capacity offshore could meet all existing scenarios for the UK's required hydrogen
488 storage, 40 – 115 TWh as suggested by Electricity System Operator (2023) and Cárdenas et al.
489 (2021).

490 The basin wide and sub-regional investigations demonstrate there are up to 10's of PWh of
491 potential storage within the Southern North Sea for hydrogen (Figures. 5-6), an order of
492 magnitude greater than is required, and several times larger than the estimate working
493 capacity of depleted gas fields and aquifers in the same location (2661 TWh) (Jahanbakhsh et
494 al., 2024). The p50 of possible cavern locations estimated is 199,692 (Basin Wide geological
495 model) and 36,331 (Sub-Regional geological model), clearly providing extensive possible sites
496 for consideration for development in the future. When the total number of caverns is so high,
497 the total capacity across is largely irrelevant. Value from our Basin wide and Sub-Regional
498 results hence does not come from the capacity of hydrogen storage, but rather the cavern
499 number and placement, both factors being required for energy systems planning (Samsatli
500 and Samsatli, 2019). At a block scale the results from using higher resolution geological
501 models (Figures 7 – 11) demonstrate that areas equivalent to individual licence areas (average
502 115 km², largest 250 km²) the number of feasible cavern locations, and the total capacity are
503 far greater than current scenarios for the UK's required hydrogen storage (Cárdenas et al.,
504 2021; Electricity System Operator, 2023).

505 By considering clusters of caverns (e.g. Figure. 11) we make use of the spatial outputs of the
506 model to compare the merits of different cluster development locations. We examine
507 conceptual salt cavern cluster developments in the layered evaporite area, using the variable
508 cavern montecarlo iteration closest to the p50 capacity value (Figure 8, 11) as the base case.
509 The development concepts, although lacking integral detailed engineering constraints built
510 in, are limited to spatial extents that are feasible with existing technologies (Energy
511 Technologies Institute, 2013). The principal consideration is the step out distance from a fixed
512 offshore infrastructure point, for which we have considered distances of 1.5km and 3km. The
513 distance from the fixed centre point to the centre of each theoretical cavern location is
514 considered a viable representation of either a) a seabed pipeline distance to tie back
515 individual caverns, or b) the drilling of a deviated well with a step out. The examples shown
516 are to demonstrate the value of the outputs from the workflow we have developed. Both
517 cavern cluster concepts, E and D, had sufficient capacity to match the minimum required
518 energy storage set by Cárdenas et al. (2021), however these both still had very large number

519 of caverns present >50. Cluster A, however, with 26.9 TWh potential is close to the 42 TWh
520 requirement, with only 22 caverns and 22.3km of pipeline, a typical salt cavern cluster
521 development consists of up to 35 caverns (Gillhaus, 2007).

522 **Comparison to other studies**

523 Previous studies have evaluated the offshore storage capacities for salt caverns in the
524 Southern North Sea. We compare our results to these (Appendix - Table. E). Previous studies
525 suggest there is also greater than required energy storage capacity within the both the
526 onshore and offshore salt basins domains.

527 The results of our study are in line with Caglayan et al. (2020) indicating there are PWh's of
528 potential storage within the offshore of the UK in the Southern North Sea. Caglayan et al.
529 (2020) only places cavern locations within 47 salt structures within the Southern North Sea,
530 whereas our salt structure maps have 42 unique structures within our sub-regional depth
531 model, which may account for the differences. These values suggest the Southern North Sea's
532 capacity for LDES in salt caverns far exceeds any onshore basin within the UK (Appendix -
533 Table. E)

534 Whilst basin wide capacity may be useful to benchmark one basin against another, all the
535 estimates demonstrate that the total of all possible cavern locations far exceeds the UK
536 storage requirements (Appendix - Table. E). For geographic areas with laterally extensive salt,
537 the issues that are most pertinent are not related to total capacity, but rather to identifying
538 the optimum geographic location of development clusters relative to other infrastructure.
539 Our workflow allows for this geospatial investigation. This has implications for the
540 development of energy production infrastructure, such as industrial clusters, marine
541 renewable infrastructure and hydrogen production facilities, because the proximity of energy
542 storage, production and usage are important factors in considering whether sites next to each
543 other can be advantageous (Walsh et al., 2023). It can also aid with dictating the ease of
544 development for the caverns, for example, how many caverns can be emplaced in a suitable
545 shallow offshore setting or within a set buffer distance of previously mentioned
546 infrastructure.

547 **Sensitivity analysis of salt cavern site capacity**

548 Both salt cavern cluster sites are most sensitive to insolubility content and as such, is a key
549 parameter to reduce uncertainty. The model used within the sensitivity analysis relied upon
550 data from the entire basin area, refining this for site-specific solubility models or using seismic
551 data for 3D quantitative interpretation of solubility content will aid in reducing uncertainty as
552 the input distribution could be reduced. Overburden pressure gradient was the second most
553 sensitive parameter for both areas, this suggests that more complex site-specific
554 geomechanical models should be incorporated to help reduce uncertainty from capacity
555 estimates. The salt wall block was not sensitive to the depth uncertainty (Figure 12A), as
556 increasing or decreasing the salt geometries made no change to the suitability of an area for
557 cavern emplacement, however, the layered evaporite area was sensitive (Figure 12B) to the
558 depth uncertainty, likely due to the top salt being close to the maximum salt depth (Appendix
559 - Table. B, Appendix. 5). Sensitivities for salt cavern emplacement will vary on a per-site basis
560 as shown in Williams et al. (2022), our findings agree with this and site-specific models for
561 both insolubility and overburden pressures should be modelled to help confine capacity
562 results.

563

564 **5.2 Limitations of workflow/approach**

565 As with any subsurface modelling method, there are limitations. We use variable cavern
566 geometries, and frequently the capacities are calculated to have volumes greater than those
567 frequently stated in literature (Appendix - Table. E). These volumes do not exceed the volume
568 of the largest documented cavern, which has a total volume of 17,000,000 m³ (670 m tall and
569 180 m diameter) (Leith, 2000). We compare the results of modifying cavern geometries while
570 keeping every other parameter the same as seen in Appendix - Table. E (Layered evaporites –
571 Variable Caverns - p50 vs layered evaporite – Fixed Caverns - p50 Models). Allowing for larger
572 and variable cavern geometries allows for higher storage capacities within an area. However,
573 there are fewer caverns placed within these runs (Appendix - Table. E), if the placement of
574 caverns was of important consideration, smaller caverns may be favoured as they allow for
575 greater opportunities in their placement. Fewer, larger caverns would allow for less drilling in
576 the development of a possible cluster, allowing the initial capex of a site to be reduced.

577 While our geological models capture the thickness changes and the 3D structures of the
578 Zechstein of the Southern North Sea, they did not incorporate the internal 3D heterogeneities
579 that may be present. For the layered evaporite area, however, we chose to take a 2D
580 approach by mapping areas of non-viability such as faults and generalised areas of
581 insolubility and removing them as deterministic nonviable areas. However, within the salt
582 structures, none-soluble stringers and complex geometries are typically associated with the
583 internal structural heterogeneity (Pichat, 2022). Imaging in salt structures is typically poor
584 both due to the complex ray paths in the crystalline structure of salt, and seismic surveys
585 often being designed to image post and pre-salt (Jones and Davison, 2014). As such the 3D
586 heterogeneity for the salt structures investigated was not incorporated within the workflow.
587 Further work could be undertaken, such as in (Teixeira et al., 2020), utilizing quantitative
588 interpretation of the seismic data to identify areas of low solubility and incorporate them into
589 the workflow.

590 Evaporite units are known to cause thermal anomalies in heat distributions within the
591 subsurface, due to their crystalline structure conducting heat energy more efficiently than the
592 surrounding lithologies (Jackson and Hudec, 2017). The increased complexity of 3D heat flow
593 makes using a geothermal gradient inappropriate for salt, with a 1D thermal or 3D heat cube
594 being more suitable. These approaches were outside the scope our work unfortunately.
595 However, with the flexibility of our workflow, had thermal modelling been within the scope
596 of this study, or been available to utilise later, it would have been straightforward to
597 incorporate this dataset within our workflow.

598 The geomechanics of cavern emplacement were not considered in detail within our workflow.
599 The distances used for geomechanical stability between caverns was taken from literature
600 and determined as suitable for our workflow development (Allen et al., 1982; Caglayan et al.,
601 2020). Area specific geomechanics models could be incorporated into our workflow for more
602 suitable cavern placement, but the development of such was outside the scope of our
603 research.

604 Despite these limitations observed in our own usage of our workflow, it has been designed in
605 such a way that it is easily modified for different geological models, parameters, or
606 uncertainties. This is seen by the number of different cases and iterations we have run, where

607 the inputs to the workflow have been modified to be more suitable with the input geological
608 model. The outputs can even be modelled such that they are plotted against the initial 3D
609 seismic data that the depth surfaces originate from, allowing for visualisation of true plotting
610 location (Appendix. 6)

611 **5.3 Veracity of data**

612 The necessity for geological models to be reliable and reproducible is essential where they
613 underpin vital developments as part of sustainable pathways and in achieving Net Zero
614 (Steventon et al., 2022). We compare the layered evaporite salt model using seismic specific
615 data (Sections 4.1.1, Figure 8) and using basin wide depth data (Section 4.1.3, Figure 10). Both
616 models use the same parameters with only the surfaces and associated depth uncertainty
617 changing (Appendix. 5). The changing of surfaces causes a number of items to be affected: 1)
618 the formation thickness changes because the basin wide data is from top to base Zechstein,
619 whereas the site-specific surfaces are from top to base Stassfurt halite (Figure 4). 2) The depth
620 to the top salt is different, with the basin wide model being shallower, allowing for more
621 viable locations. 3) The grid cell resolution is also different; Appendix. 5 shows the differences
622 in surfaces. The basin wide data results estimate 27 more caverns, 380 TWh higher capacity,
623 and an average cavern working capacity of 720 GWh higher than the specific data geological
624 model. These differences arise from the basin wide data use of the top and base Zechstein as
625 input, rather than having the specified salt target, which in turn causes the salt to be thicker,
626 allowing for larger caverns to be placed by the workflow. Using the top and base Zechstein
627 also causes non-soluble stratigraphic layers within the Zechstein, such as the Plattendolomit
628 (Figure. 2-4), to be within the area for cavern emplacement in the workflow. If a stratigraphic
629 layer, such as the Plattendolomit, were to be encountered while attempting to solution mine
630 a cavern it may cause many issues, such as cavern collapse, inability to continue solution
631 mining, contamination, or act as a porous and permeable pathway for hydrogen to escape,
632 and, as such should be avoided (Chen et al., 2018; Zhang et al., 2021; Zhu et al., 2023).
633 The public surfaces are also lower resolution with a grid cell spacing of 250 m, as opposed to
634 50m. This lower resolution leads to ineffective packing of the caverns (Figure 10A), as the grid
635 cell size is greater than the typical buffer (~100 m) between adjacent caverns. A higher
636 resolution model enables not only more potential cavern locations to be considered, but also
637 captures a higher resolution of structural variability in the geometry of the salt interval. The
638 work presented here suggests that the minimum grid cell size of the input geological model
639 is at most 4x the minimum cavern size diameter, as this will allow for every grid cell to have a
640 point with minimum overlap. If the resolution was any lower, the circles would be inefficiently
641 packed. It is advised however that grid cell resolution should be higher than this to allow for
642 more caverns than necessary to be generated, as this will lead to better cavern packing
643 (Appendix. 7).

644

645 **5.4 Importance of reproducibility and replicability**

646 Within subsurface geosciences, practical frameworks for reproducibility are in their infancy,
647 particularly where there are significant uncertainties related to data (Steventon et al., 2022).
648 In particular it has been identified that availability of data and software (including code),
649 frequently limit the possibility of reproducing studies (Ireland et al., 2023). Previous studies
650 into geological energy storage estimates rarely provide sufficient information to be
651 reproduced. This study has made available the code through a CC BY-SA so that it can be used,
652 revised, and modified, including for commercial purposes. This therefore allows others to test

653 the replicability of our method (e.g., same method, different data). As well as the method, it
654 is vital that the underlying data for studies are made available (Hardwicke et al., 2018).
655 Previous studies of geological energy storage do not provide the data used for the capacity
656 estimates, thus limiting the opportunity to examine the reliability of the estimates. In this
657 study we use data, and interpretations from existing open licence sources (NSTA), as well as
658 our own interpretations, which we also make available through CC-Y licence. This approach
659 allows for all our results to be fully reproducible and replicable.

660 The comparison shown in Appendix - Table. E highlights the importance of reproducibility and
661 reliability in studies where results may have implications for both the scientific community
662 and policy makers. The results from Caglayan et al. (2020) and Allsop et al. (2023), for the
663 same areas indicate differences of up to 3124 TWh and 11,832 TWh respectively (compared
664 with sub-regional model). With such large differences in predictions, it is important to be able
665 to understand where such differences arise from, however replicability is only viable when
666 the original data is published. While our capacity calculations are larger than the those
667 proposed in Caglayan et al. (2020), they both agree that there is PWh storage potential of
668 hydrogen within the Southern North Sea, with our sub-regional model differing by 29.5%,
669 while using different subsurface datasets (Caglayan et al. (2020) do not incorporate layered
670 evaporite domains into their geological model). Allsop et al. (2023) estimated significantly
671 different capacities in comparison to this study, for both the salt wall and the sub-regional
672 model (Appendix - Table. B,E) while using the same seismic data (2016 Southern North Sea
673 Mega-merge). They estimate that only 1485 caverns can be emplaced within the entirety of
674 sub-regional area, as opposed to 34,108 in our study, and only 105 within the Audrey salt wall
675 as opposed to the 1154 presented here (using the same cavern geometries) (Figure. 6,7).
676 Unfortunately, due to the lack of detail in the methodology and results (no geospatial data
677 regarding cavern placement) presented by Allsop et al. (2023) we were unable to make a
678 detailed comparison between each workflow and understand where these differences
679 originated. Allsop et al. (2023). This example of researchers reaching different conclusions
680 while utilising the same dataset emphasises the importance of reproducibility and
681 replicability in geoscience There are many studies in the geoscience community, where the
682 results are unable to be reproduced or replicated (Ireland et al., 2023). When all aspects of
683 research are open this improves their trustworthiness (Rosman et al., 2022), which is essential
684 if findings are to inform policy or aspects of national planning, such as energy systems (UK
685 Government, 2012).

686 **5.5 Energy system integration.**

687 The outputs generated from our workflow are such that they contain individual cavern
688 locations, specification, and capacities. These outputs can be used as inputs into further
689 energy systems modelling that include storage e.g Sunny et al. (2020). Energy system models
690 and energy value chain studies, while having offshore energy generation within their models,
691 typically implement storage opportunities within the onshore domain, not offshore, limiting
692 opportunity and constricting possible energy solutions (Samsatli and Samsatli, 2019). Aiding
693 in the design of energy systems can occur at all scales because of the different geological
694 models that were run through our workflow (broad whole basin geological models to site
695 specific models).

696 The geographic results, both individual caverns and conceptual clusters can be reviewed with
697 respect to important energy infrastructure. For example, Figure. 13 shows the number of
698 caverns and capacity within 20km radius of existing and planned offshore wind developments

699 in the Southern North Sea. Of the 32 developments, 15 have > 1000 viable cavern locations
700 and 15 have over 500 TWh of viable hydrogen capacity (Figure. 13). We can also examine the
701 setting of cavern locations, such as water depth or distance from the coastline, both which
702 could impact the development cost (Energy Technologies Institute, 2013). All cavern locations
703 are situated in under 100 m water depth, which means all could be developed by a jack-up
704 ship (limits are typically 120m). There are 21,000 possible cavern locations within 10 km and
705 37,000 within 20 km of the east coast (Basin wide model).

706 These are some possible examples as to how the output from this study and our workflow
707 could be integrated into energy systems design. While our brief overview of this is simplistic,
708 our data could be used for much more complex analysis because of the level of information
709 associated with each cavern generated.

710

711 **5.6 Offshore salt caverns for LDES**

712 To date, all salt caverns have been emplaced onshore, however offshore salt cavern projects
713 have been proposed before (Evans and Holloway, 2009). We have demonstrated that not only
714 does the total capacity available exceed current estimates for storage, but that the number
715 of viable geographic locations offshore has the potential to provide effective integration with
716 current and future marine renewable infrastructure (Figures. 5,6,13). The integration of salt
717 cavern clusters for LDES could provide greater flexibility and variability in the generation of
718 energy from offshore renewables (Arellano-Prieto et al., 2022). The idealised location for
719 caverns is next to hydrogen production hubs, those generating either blue or green hydrogen,
720 optimising the integration, flexibility and transport of hydrogen from production to storage
721 (Walsh et al., 2023).

722 Subsurface/infrastructure work that occurs offshore has costs associated with it that are
723 higher than those that occur onshore, for example wind turbines are 50% more expensive
724 offshore than onshore (Bilgili et al., 2011). Savings might be possible in regard to salt caverns,
725 as disposal of brine produced by the creation of the salt caverns into the sea will be more cost
726 effective than the cost of transporting the brine onshore. The cost of pipelines will need to be
727 a key aspect of site consideration as they will be a significant component of the CAPEX costs.
728 Throughout our theoretical salt cavern sites, we have modelled the possible distances of
729 pipeline for a single cluster to get reasonable estimates as to what may be required, however
730 a more thorough specific investigation into this will be needed.

731 Alternate energy vectors could be stored within salt caverns to alleviate carbon emissions in
732 other industries. Global shipping accounts for 2% of global carbon dioxide emissions, both
733 ammonia and methanol have been suggested as replacement 0 emission fuel sources
734 (Gallucci, 2021; Svanberg et al., 2018). At the average internal pressure/temperature
735 conditions of the salt caverns from our basin wide study (64 °c and 36.2 MPa), ammonia would
736 be in its super critical phase and methanol would be in its liquid phase (National Institute of
737 Standards and Technology, 2023). Ammonia has previously been suggested as storable within
738 salt caverns (Adams and Cottle, 1954). Combining storage and offshore production of these
739 zero emission fuels would allow for an fully integrated green ship refuelling ecosystem. If salt
740 caverns are unsuitable for these energy vectors for reasons we may have missed, hydrogen
741 stored within the caverns could be used as a feedstock for a surface production facility for
742 these possible fuels.

743 **6. Conclusion**

744 Within this paper we have demonstrated our proposed workflow using several geological
745 models and parameters. We position this workflow at the pre-feasibility stage of an area for
746 the investigation placement of salt caverns. The workflow takes a geological model as an input
747 and outputs valid salt cavern locations alongside capacity estimates. The workflow has been
748 designed that such that any parameter and variables can be changed to suit the geological
749 model and area of interest, even allowing the chosen energy vector to be altered. The
750 workflow allows for the input of not only deterministic values but stochastic values, allowing
751 to compensate for the uncertainty typically associated with geological models of the
752 subsurface.

753 From our workflow we produce realistic theoretical salt cavern clusters that help to show how
754 the results from our model could be used to develop such a cluster. The capacity results show
755 that a single large offshore cavern cluster (with a 3km diameter AOI) may have enough
756 hydrogen storage capacity to meet the UK's long duration energy storage requirements in
757 full. The workflow and associated data should be used to aid site planners or policy setters to
758 making further decisions regarding hydrogen storage offshore using salt caverns.

759 The offshore domain is often not considered when deciding where LDES should be placed.
760 We have demonstrated that the offshore of the UK is a suitable location, with over 199,000
761 locations of caverns and PWh scale capacity for hydrogen. This viability of the offshore
762 domains opens possible co-location with offshore energy production hubs, allowing for the
763 UK to have a full green energy production hub operating offshore.

764 We also compare our results against other studies to emphasise how important it is to have
765 a reproducible and replicable methodology. All code, data and interpretations used within
766 this study are supplied within the data repository.

767

768 **Figure Captions**

769 Figure. 1 - Location map of areas of interest (Aols), offshore East coast of the UK. Aol locations
770 are labelled and shown on the map. Well data used in the 'Block – Layered Evaporite' area is
771 marked on, as well as seismic cross sections (Figure. 3). Map 2, (top left) details the extent of
772 the study areas in respect to the whole of the UK and Northern Europe.

773 Figure. 2 - Cartoon schematic geological cross-section of emplaced salt caverns (Not to
774 scale). Important parameters (both inputs and calculations) for characterizing a salt cavern
775 site have been labelled A – k, and overburden characterization 1 - 7. The right diagram
776 shows an individual cavern and the parameters considered for individual cavern placement.

777 Figure. 3 - A) Example seismic cross section from the 'Block – Layered Evaporite' Aol (Seismic
778 Survey MA933F0002), running North to South, A – A' (Figure. 1), in TWT, key reflections have
779 been marked on.

780 Figure 4 – Petrophysical logs (well 41/05-1, Figure. 1), GR (gamma-ray), DT (sonic), Rhob
781 (density), interpreted lithology log is present. Calculated synthetic seismic wiggle overlying
782 seismic trace from seismic survey MA933F002 and interpreted key stratigraphic boundaries.

783 Figure 5 – A) Cavern placement map ‘Basin Wide’ Aol, fixed cavern geometries. Geospatial
784 placement represents the output model from the workflow with the closest total hydrogen
785 capacity to the calculated p50 (Iteration 149/2500). A total of 200570 caverns are placed,
786 with a sum of >61.9 PWh of hydrogen storage capacity. B) Histogram of total hydrogen
787 capacities for each iteration of the Montecarlo simulation (2500 iterations). C) Histogram of
788 total cavern number for each iteration of the Montecarlo simulation (2500 iterations).

789 Figure 6 – A) Cavern placement map ‘Sub-regional’ Aol, fixed cavern geometries. Geospatial
790 placement represents the output model from the workflow with the closest total hydrogen
791 capacity to the calculated p50 (Iteration 141/2500). A total of 37,518 caverns are placed,
792 with a sum of 12.1 PWh of hydrogen storage capacity. B) Histogram of total hydrogen
793 capacities for each iteration of the Montecarlo simulation (2500 iterations). C) Histogram of
794 total cavern number for each iteration of the Montecarlo simulation (2500 iterations).

795 Figure 7 – A) Cavern placement map ‘Block Specific – Salt Wall’ Aol, variable cavern
796 geometries. Geospatial placement represents the output model from the workflow with the
797 closest total hydrogen capacity to the calculated p50 (Iteration 1248/2500). A total of 409
798 caverns are placed, with a sum of 731.2 TWh of hydrogen storage capacity. B) Histogram of
799 total hydrogen capacities for each iteration of the Montecarlo simulation (2500 iterations). C)
800 Cavern placement map ‘Block Specific – Salt Wall’ Aol, fixed cavern geometries. Geospatial
801 placement represents the output model from the workflow with the closest total hydrogen
802 capacity to the calculated p50 (Iteration 149/2500). A total of 1152 caverns are placed, with
803 a sum of 225.5 TWh of hydrogen storage capacity. D) Histogram of total hydrogen capacities
804 for each iteration of the Montecarlo simulation (2500 iterations).

805 Figure 8 – Cavern placement map ‘Block Specific – Layered Evaporite’ Aol, variable cavern
806 geometries. Geospatial placement represents the output model from the workflow with the
807 closest total hydrogen capacity to the calculated p90 (A, Iteration: 1590), p50(B, Iteration:
808 175), and p10 (C, Iteration: 1128). D) Histogram of total hydrogen capacities for each iteration
809 of the Montecarlo simulation (2500 iterations). E) Histogram of total cavern number for each
810 iteration of the Montecarlo simulation (2500 iterations).

811 Figure 9 – A) Cavern placement map ‘Block Specific – Layered Evaporite’ Aol with fixed
812 geometries. Geospatial placement represents the output model from the workflow with the
813 closest total hydrogen capacity to the calculated p50 (Iteration 1537/2500). A total of 839
814 caverns are placed, with a sum of 260.3 TWh of hydrogen storage capacity. B) Histogram of
815 total hydrogen capacities for each iteration of the Montecarlo simulation (2500 iterations). C)
816 Histogram of total cavern number for each iteration of the Montecarlo simulation (2500
817 iterations).

818 Figure 10 – A) Cavern placement map ‘Block Specific – Layered Evaporite’ Aol , variable cavern
819 geometries using ‘Basin Wide’ Aol depth surfaces. Geospatial placement represents the
820 output model from the workflow with the closest total hydrogen capacity to the calculated
821 p50 (Iteration 1085/2500). A total of 494 caverns are placed, with a sum of 798.7 TWh of
822 hydrogen storage capacity. B) Histogram of total hydrogen capacities for each iteration of the
823 Montecarlo simulation (2500 iterations). C) Histogram of total cavern number for each
824 iteration of the Montecarlo simulation (2500 iterations). D) Seismic cross section running
825 West to East, B – B' (Figure. 1,11A), in TVD (m). Stassfurt halite surfaces interpreted from
826 seismic survey MA933F002 and depth converted are present, Green (Top Stassfurt Halite) and

827 Red (Base Stassfurt halite / Top basal polyhalite). Blue and orange lines represent publicly
 828 available depth surfaces acquired from the NSTA of the top and base Zechstein, used for the
 829 'Basin Wide' Aol geological model.

830 Figure 11 - Salt cavern cluster concept play map. Base salt cavern map is the representative
 831 p50 of the 'Block - Layered Evaporite' Aol variable cavern model (Figure. 8 B). 5 possible
 832 cavern cluster concepts are described A) Max hydrogen capacity within a 1.5 km radius. B)
 833 Maximum cavern number within a 1.5 km radius. C) 1.5km radius placed upon existing
 834 infrastructure (wellbore 41/05-1, Figures. 1, 4). D) Max hydrogen capacity within a 3 km
 835 radius. E) Maximum cavern number within a 3 km radius. Radiuses were chosen as such to
 836 mimic offshore infrastructure.

837 Figure 12. Sobol sensitivity results of input parameters for A) The salt wall with variable
 838 caverns (4.3.1.1); and B) The layered evaporite with variable caverns (4.3.2.1)

839 Figure 13 – Windfarms located within the 'Basin Wide' Aol (Figure. 5), plotted against viable
 840 cavern number and total hydrogen storage capacity within a 20km buffer of the windfarm
 841 site (Basin Wide results used (Section 4.1.1)).

842 **Tables**

843 Table 1 – Results of Montecarlo simulation, iterations closest to P values from Layered
 844 evaporite – Variable cavern geometries

Outcome	Total Working hydrogen Capacity (TWh)	Total Cavern Number	Average Cavern Working Capacity (GWh)	Smallest Cavern Working Capacity (GWh)	Largest Cavern Working Capacity (GWh)	Energy Density (TWh/Km ²)
P90 (Iteration: 1590)	387.5	337	1149.9	309.7	2215.1	1.72
P50 (Iteration: 175)	419.2	467	897.6	259.5	1990.2	1.86
P10 (Iteration: 1128)	449.5	478	940.4	255.3	1991.8	2.00

845

846 Table 2. Theoretical salt cavern cluster information (Figure. 11)

Cluster	Total Hydrogen Capacity (TWh)	Cavern Number	Pipeline / Deviation length (km)
A – Max Hydrogen Capacity 1.5km radius	26.9	22	22.3
B – Maximum Caverns (1.5km radius)	10.2	28	28.5
C – On existing well	18.7	19	18.4

D – Max Hydrogen Capacity (3 km radius)	84.4	72	141.5
E – B – Maximum Caverns (3km radius)	51.2	91	181.6

847

848 **Data Availability**

849

850 All data generated within this study is available through a data repository located at
851 <https://doi.org/10.25405/data.ncl.c.7016283> and is available under a CC BY-SA license. The
852 code/workflow within this study is available under open access licence GPL 3.0+ and can be
853 found as an interactive python notebook either in the data repository or on the primary
854 authors github (<https://github.com/Hector-Barn/Tools>). The interactive python notebook will
855 be kept-up to date at github. The jupyter notebook present within the data repository acts as
856 an archive for the code used within this study for repeatability reasons.

857 All Montecarlo runs are also available as a CSV file to cross reference shown data and
858 calculated and are available in alongside the geospatial results in the data repo.

859 The Basin wide surfaces used within this study are available through the following link NSTA
860 Regional surfaces (<https://hub.arcgis.com/documents/NSTAUTHORITY::nsta-and-lloyds-register-sns-regional-geological-mapsa-open-source/about>). (Basin wide open licence
861 geological interpretations are available for the Southern North Sea).
862 Seismic survey and well data used are available through the NSTA's National Data Repository
863 (<https://ndr.nstauthority.co.uk/>)
864

865 The CGG geothermal database used can be found through the following UK gov link
866 (<https://www.data.gov.uk/dataset/6cf03f34-12af-41f4-bf9d-1c305a1c5f12/cgg-geothermal-database>)
867

868 **Acknowledgements**

869 Hector Barnett's PhD is funded through the Centre for Doctoral Training (CDT) in Geoscience
870 and the Low Carbon Energy Transition. Seismic and well data were provided by the North Sea
871 Transition Authority under an Open Government Licence. Bathymetry data was provided by
872 The European Marine Observation and Data Network. Data were interpreted using SLB's
873 Petrel and Techlog software which was provided under an academic licence. The code,
874 geological models and outputs from this study are available through data.ncl.ac.uk
875 [<https://doi.org/10.25405/data.ncl.c.7016283>]

876 We acknowledge and are grateful to SLB for providing academic licenses for their Petrel and
877 Techlog software which was used to visualise and interrogate the seismic data.

878 This work is currently available as a preprint on EarthArXiv (Barnett et al., 2024)

879 **Bibliography**

880 Adams, L., & Cottle, J. (1954). *Underground storage of ammonia and its recovery.*

881 Allen, K. (1972). Eminence Dome - Natural-Gas Storage In Salt Comes of Age. *Journal of Petroleum*
882 *Technology*, 24(11), 1299-1301. <https://doi.org/10.2118/3433-pa>

883 Allen, R. D., Doherty, T. J., & THorns, R. L. (1982). *Geotechnical Factors and Guidelines for Storage of*
884 *Compressed Air in Solution Mined Salt Cavities*.

885 Allsop, C., Yfantis, G., Passaris, E., & Edlmann, K. (2023). Utilizing publicly available datasets for
886 identifying offshore salt strata and developing salt caverns for hydrogen storage. *Geological*
887 *Society, London, Special Publications*, 528(1), 139-169. [https://doi.org/10.1144/sp528-2022-](https://doi.org/10.1144/sp528-2022-82)
888 [82](https://doi.org/10.1144/sp528-2022-82)

889 Arellano-Prieto, Y., Chavez-Panduro, E., Salvo Rossi, P., & Finotti, F. (2022). Energy Storage Solutions
890 for Offshore Applications. *Energies*, 15(17). <https://doi.org/10.3390/en15176153>

891 Barnett, H., Ireland, M., & van der Land, C. (2024). Capturing geological uncertainty in salt cavern
892 developments for hydrogen 1 storage: Case study from Southern North Sea. . *EarthArXiv*.
893 <https://doi.org/10.31223/x5pq4c>

894 Barnett, H. G., Ireland, M. T., & van der Land, C. (2023). Characterising the internal structural
895 complexity of the Southern North Sea Zechstein Supergroup Evaporites. *Basin Research*,
896 35(5), 1651-1673. <https://doi.org/10.1111/bre.12768>

897 Bauer, S., Beyer, C., Dethlefsen, F., Dietrich, P., Duttmann, R., Ebert, M., Feeser, V., Görke, U., Köber,
898 R., Kolditz, O., Rabbel, W., Schanz, T., Schäfer, D., Würdemann, H., & Dahmke, A. (2013).
899 Impacts of the use of the geological subsurface for energy storage: an investigation concept.
900 *Environmental Earth Sciences*, 70(8), 3935-3943. [https://doi.org/10.1007/s12665-013-2883-](https://doi.org/10.1007/s12665-013-2883-0)
901 [0](https://doi.org/10.1007/s12665-013-2883-0)

902 Bérest, P., Brouard, B., Hévin, G., & Réveillère, A. (2021). Tightness of Salt Caverns Used for
903 Hydrogen Storage. 55th U.S. Rock Mechanics/Geomechanics Symposium,

904 Bilgili, M., Yasar, A., & Simsek, E. (2011). Offshore wind power development in Europe and its
905 comparison with onshore counterpart. *Renewable and Sustainable Energy Reviews*, 15(2),
906 905-915. <https://doi.org/10.1016/j.rser.2010.11.006>

907 Bourke, L., Delfiner, P., Felt, T., Grace, M., Luthi, S., Serra, O., & Standen, E. (1989). Using formation
908 Microscanner images: The (Schlumberger) Technical Review. In (pp. 16 - 40).

909 Caglayan, D. G., Weber, N., Heinrichs, H. U., Linßen, J., Robinius, M., Kukla, P. A., & Stolten, D. (2020).
910 Technical potential of salt caverns for hydrogen storage in Europe. *International Journal of*
911 *Hydrogen Energy*, 45(11), 6793-6805. <https://doi.org/10.1016/j.ijhydene.2019.12.161>

912 Calado, G., & Castro, R. (2021). Hydrogen Production from Offshore Wind Parks: Current Situation
913 and Future Perspectives. *Applied Sciences*, 11(12). <https://doi.org/10.3390/app11125561>

914 Cárdenas, B., Swinfen-Styles, L., Rouse, J., Hoskin, A., Xu, W., & Garvey, S. D. (2021). Energy storage
915 capacity vs. renewable penetration: A study for the UK. *Renewable Energy*, 171, 849-867.
916 <https://doi.org/10.1016/j.renene.2021.02.149>

917 Centrica. (2023). *Centrica bolsters UK's energy security by doubling Rough storage capacity*.
918 Retrieved 27/09/2023 from [https://www.centrica.com/media-centre/news/2023/centrica-](https://www.centrica.com/media-centre/news/2023/centrica-bolsters-uk-s-energy-security-by-doubling-rough-storage-capacity/)
919 [bolsters-uk-s-energy-security-by-doubling-rough-storage-capacity/](https://www.centrica.com/media-centre/news/2023/centrica-bolsters-uk-s-energy-security-by-doubling-rough-storage-capacity/)

920 Chen, X., Li, Y., Liu, W., Ma, H., Ma, J., Shi, X., & Yang, C. (2018). Study on Sealing Failure of Wellbore
921 in Bedded Salt Cavern Gas Storage. *Rock Mechanics and Rock Engineering*, 52(1), 215-228.
922 <https://doi.org/10.1007/s00603-018-1571-5>

923 Costa, P. V. M., Costa, A. M., Szklo, A., Branco, D. C., Freitas, M., & Rosa, L. P. (2017). UGS in giant
924 offshore salt caverns to substitute the actual Brazilian NG storage in LNG vessels. *Journal of*
925 *Natural Gas Science and Engineering*, 46, 451-476.
926 <https://doi.org/10.1016/j.jngse.2017.06.035>

927 Crotagino, F., Schneider, G.-S., & Evans, D. J. (2017). Renewable energy storage in geological
928 formations. *Proceedings of the Institution of Mechanical Engineers, Part A: Journal of Power*
929 *and Energy*, 232(1), 100-114. <https://doi.org/10.1177/0957650917731181>

930 Department for Environment Food and Rural Affairs. (2014). *Section_3.2_Temperature_and_Salinity*.
931 Retrieved 18/12/2023 from

932 https://webarchive.nationalarchives.gov.uk/ukgwa/20141203184215/http://chartingprogress.defra.gov.uk/feeder/Section_3.2_Temperature_and_Salinity.pdf

933

934 Doornenbal, J. C., Kombrink, H., Bouroullec, R., Dalman, R. A. F., De Bruin, G., Geel, C. R., Houben, A.

935 J. P., Jaarsma, B., Juez-Larré, J., Kortekaas, M., Mijnlief, H. F., Nelskamp, S., Pharaoh, T. C.,

936 Ten Veen, J. H., Ter Borgh, M., Van Ojik, K., Verreussel, R. M. C. H., Verweij, J. M., & Vis, G. J.

937 (2019). New insights on subsurface energy resources in the Southern North Sea Basin area.

938 *Geological Society, London, Special Publications*. <https://doi.org/10.1144/sp494-2018-178>

939 Dowling, J. A., Rinaldi, K. Z., Ruggles, T. H., Davis, S. J., Yuan, M., Tong, F., Lewis, N. S., & Caldeira, K.

940 (2020). Role of Long-Duration Energy Storage in Variable Renewable Electricity Systems.

941 *Joule*, 4(9), 1907-1928. <https://doi.org/10.1016/j.joule.2020.07.007>

942 Eising, J., Brouwer, F., & Bernd, A. (2021). *Appendix: Risk analysis of worldwide salt cavern storage*

943 [Vrije Universiteit Amsterdam].

944 Elam, S. D. (2007). *First Gas after 40 Years – The Geophysical Challenges of the Saturn Gas Complex*

945 AAPG Annual Convention 2007, Long Beach, California.

946 Electricity System Operator. (2023). *Future Energy Scenarios*. Retrieved from

947 <https://www.nationalgrideso.com/document/283101/download>

948 Energy Technologies Institute. (2013). *Hydrogen Storage and Flexible Turbine Systems WP2 Report –*

949 *Hydrogen Storage* (Carbon Capture and Storage - Hydrogen Turbines, Issue.

950 Evans, D. J. (2007). *An appraisal of Underground Gas Storage technologies and incidents, for the*

951 *development of*

952 *risk assessment methodology*. B. G. Survey.

953 Evans, D. J., & Holloway, S. (2009). A review of onshore UK salt deposits and their potential for

954 underground gas storage. *Geological Society, London, Special Publications*, 313(1), 39-80.

955 <https://doi.org/10.1144/sp313.5>

956 François, L. L. (2021, November 2021). *Four Ways to Store Large Quantities of Hydrogen* Abu Dhabi

957 International Petroleum Exhibition & Conference, Abu Dhabi, UAE.

958 Gallucci, M. (2021). *The Ammonia Solution: Ammonia engines and fuel cells in cargo ships could slash*

959 *their carbon emissions*.

960 Gillhaus, A. (2007). *Natural gas storage in salt caverns present trends in Europe*

961 Glennie, K. W. (1998). *Petroleum Geology of the North Sea: Basic Concepts and Recent Advances* (4

962 ed.). Blackwell Science. <https://doi.org/10.1002/9781444313413>

963 Grant, R. J., Underhill, J. R., Hernández-Casado, J., Barker, S. M., & Jamieson, R. J. (2019). Upper

964 Permian Zechstein Supergroup carbonate-evaporite platform palaeomorphology in the UK

965 Southern North Sea. *Marine and Petroleum Geology*, 100, 484-518.

966 <https://doi.org/10.1016/j.marpetgeo.2017.11.029>

967 Hardwicke, T. E., Mathur, M. B., MacDonald, K., Nilsonne, G., Banks, G. C., Kidwell, M. C., Hofelich

968 Mohr, A., Clayton, E., Yoon, E. J., Henry Tessler, M., Lenne, R. L., Altman, S., Long, B., &

969 Frank, M. C. (2018). Data availability, reusability, and analytic reproducibility: evaluating the

970 impact of a mandatory open data policy at the journal

971 Cognition. *Royal Society Open Science*, 5(8). <https://doi.org/10.1098/rsos.180448>

972 Hassanpouryouzband, A., Adie, K., Cowen, T., Thaysen, E. M., Heinemann, N., Butler, I. B., Wilkinson,

973 M., & Edmann, K. (2022). Geological Hydrogen Storage: Geochemical Reactivity of Hydrogen

974 with Sandstone Reservoirs. *ACS Energy Letters*, 7(7), 2203-2210.

975 <https://doi.org/10.1021/acsenergylett.2c01024>

976 Heinemann, N., Alcalde, J., Miocic, J. M., Hangx, S. J. T., Kallmeyer, J., Ostertag-Henning, C.,

977 Hassanpouryouzband, A., Thaysen, E. M., Strobel, G. J., Schmidt-Hattenberger, C., Edmann,

978 K., Wilkinson, M., Bentham, M., Stuart Haszeldine, R., Carbonell, R., & Rudloff, A. (2021).

979 Enabling large-scale hydrogen storage in porous media – the scientific challenges. *Energy &*

980 *Environmental Science*, 14(2), 853-864. <https://doi.org/10.1039/d0ee03536j>

981 Heinemann, N., Booth, M. G., Haszeldine, R. S., Wilkinson, M., Scafidi, J., & Edlmann, K. (2018).
982 Hydrogen storage in porous geological formations – onshore play opportunities in the
983 midland valley (Scotland, UK). *International Journal of Hydrogen Energy*, 43(45), 20861-
984 20874. <https://doi.org/10.1016/j.ijhydene.2018.09.149>

985 Herman, J., & Usher, W. (2017). SALib: An open-source Python library for Sensitivity Analysis. *The*
986 *Journal of Open Source Software*, 2(9). <https://doi.org/10.21105/joss.00097>

987 Hunter, C. A., Penev, M. M., Reznicek, E. P., Eichman, J., Rustagi, N., & Baldwin, S. F. (2021). Techno-
988 economic analysis of long-duration energy storage and flexible power generation
989 technologies to support high-variable renewable energy grids. *Joule*, 5(8), 2077-2101.
990 <https://doi.org/10.1016/j.joule.2021.06.018>

991 HyUnder. (2013). *D3.1 - Assessment of the potential, the actors and relevant business cases for large*
992 *scale and seasonal storage of renewable electricity by hydrogen underground storage in Europe.*
993 Ireland, M., Algarabel, G., Steventon, M., & Munafò, M. (2023). How reproducible and reliable is
994 geophysical research? *Seismica*, 2(1). <https://doi.org/10.26443/seismica.v2i1.278>

995 Iwanaga, T., Usher, W., & Herman, J. (2022). Toward SALib 2.0: Advancing the accessibility and
996 interpretability of global sensitivity analyses. *Socio-Environmental Systems Modelling*, 4.
997 <https://doi.org/10.18174/sesmo.18155>

998 Jackson, M. P. A., & Hudec, M. R. (2017). *Salt Tectonics*. Cambridge University Press.
999 <https://doi.org/doi.org/10.1017/9781139003988>

1000 Jahanbakhsh, A., Louis Potapov-Crighton, A., Mosallanezhad, A., Tohidi Kaloorazi, N., & Maroto-
1001 Valer, M. M. (2024). Underground hydrogen storage: A UK perspective. *Renewable and*
1002 *Sustainable Energy Reviews*, 189. <https://doi.org/10.1016/j.rser.2023.114001>

1003 Johnson, Warrington, & Stoker. (1993). *Lithostratigraphic Nomenclature of the UK North Sea:*
1004 *Permian and Triassic of the Southern North Sea v. 6*. British Geological Survey.

1005 Jones, I. F., & Davison, I. (2014). Seismic imaging in and around salt bodies. *Interpretation*, 2(4), SL1-
1006 SL20. <https://doi.org/10.1190/int-2014-0033.1>

1007 King, M., Jain, A., Bhakar, R., Mathur, J., & Wang, J. (2021). Overview of current compressed air
1008 energy storage projects and analysis of the potential underground storage capacity in India
1009 and the UK. *Renewable and Sustainable Energy Reviews*, 139.
1010 <https://doi.org/10.1016/j.rser.2021.110705>

1011 Kueppers, M., Paredes Pineda, S. N., Metzger, M., Huber, M., Paulus, S., Heger, H. J., & Niessen, S.
1012 (2021). Decarbonization pathways of worldwide energy systems – Definition and modeling
1013 of archetypes. *Applied Energy*, 285. <https://doi.org/10.1016/j.apenergy.2021.116438>

1014 Landinger, H., & Crotogino, F. (2007). The role of large-scale hydrogen storage for future renewable
1015 energy utilisation. Second International Renewable Energy Storage Conference (IRES II),
1016 Leith, W. (2000). Geologic and engineering constraints on the feasibility of clandestine nuclear
1017 testing by decoupling in large underground cavities. <https://doi.org/10.3133/ofr0128>

1018 Lokhorst, A., & Wildenborg, T. (2006). Introduction on CO2 Geological Storage - Classification of
1019 Storage Options. *Oil & Gas Science and Technology*, 60(3), 513-515.
1020 <https://doi.org/10.2516/ogst:2005033>

1021 Ma, H., Wei, X., Shi, X., Liang, X., Bai, W., & Ge, L. (2022). Evaluation Methods of Salt Pillar Stability of
1022 Salt Cavern Energy Storage. *Energies*, 15(20). <https://doi.org/10.3390/en15207570>

1023 McNamara, J. W., DeAngelis, V., Byrne, R. H., Benson, A., Chalamala, B. R., & Masiello, R. (2022).
1024 Long-duration energy storage in a decarbonized future: Policy gaps, needs, and
1025 opportunities. *MRS Energy & Sustainability*, 9(2), 142-170. <https://doi.org/10.1557/s43581-022-00037-9>

1026
1027 Muhammed, N. S., Haq, B., Al Shehri, D., Al-Ahmed, A., Rahman, M. M., & Zaman, E. (2022). A review
1028 on underground hydrogen storage: Insight into geological sites, influencing factors and
1029 future outlook. *Energy Reports*, 8, 461-499. <https://doi.org/10.1016/j.egyr.2021.12.002>

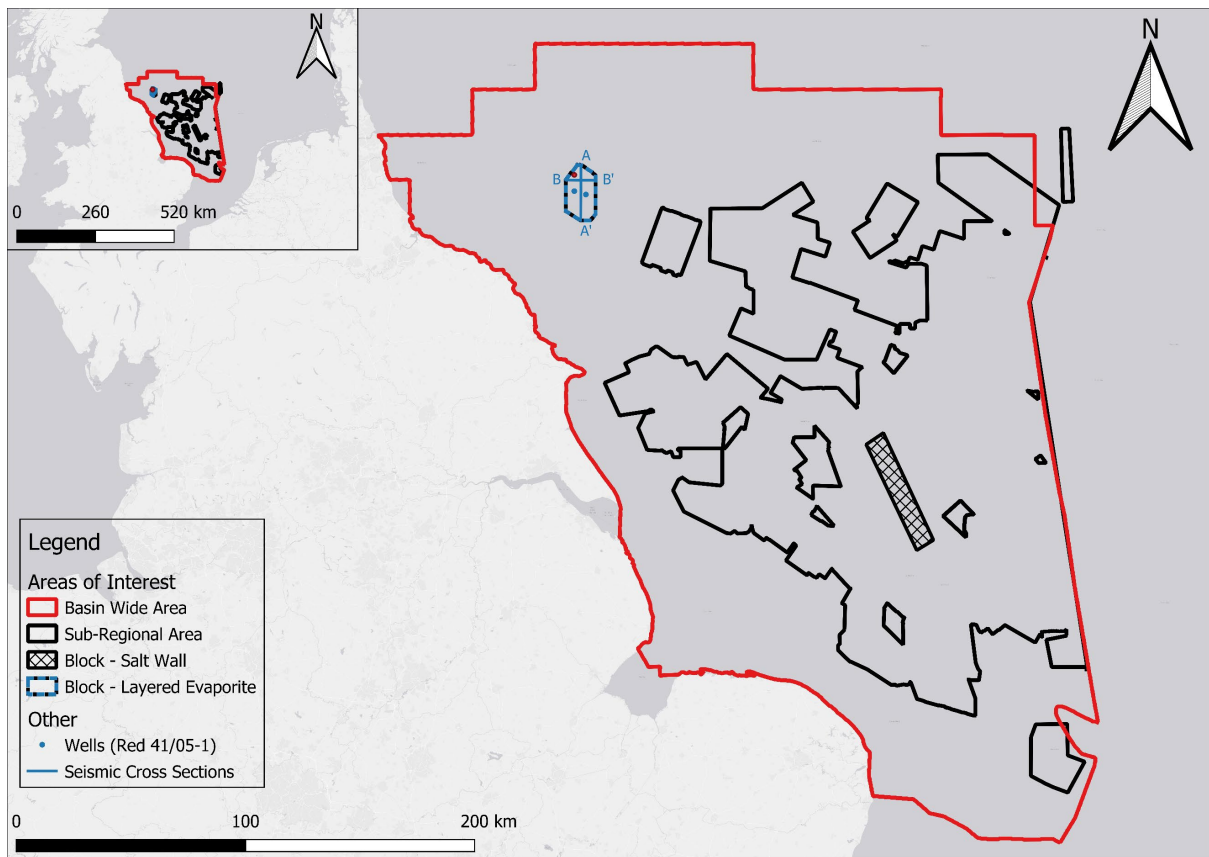
1030 National Institute of Standards and Technology. (2023). U.S. Department of Commerce.

- 1031 North Sea Transition Authority. (2022). *Gas storage and unloading*.
 1032 [https://www.nstauthority.co.uk/regulatory-information/gas-storage-and-](https://www.nstauthority.co.uk/regulatory-information/gas-storage-and-unloading/#:~:text=Award%20of%20Gas%20Storage%20Licence%20%2D%20July%202022,in%20the%20Southern%20North%20Sea.)
 1033 [unloading/#:~:text=Award%20of%20Gas%20Storage%20Licence%20%2D%20July%202022,in](https://www.nstauthority.co.uk/regulatory-information/gas-storage-and-unloading/#:~:text=Award%20of%20Gas%20Storage%20Licence%20%2D%20July%202022,in%20the%20Southern%20North%20Sea.)
 1034 [%20the%20Southern%20North%20Sea.](https://www.nstauthority.co.uk/regulatory-information/gas-storage-and-unloading/#:~:text=Award%20of%20Gas%20Storage%20Licence%20%2D%20July%202022,in%20the%20Southern%20North%20Sea.)
- 1035 Oil and Gas Authority. (2021). *OGA Strategy*. [https://www.nstauthority.co.uk/media/7105/the-oga-](https://www.nstauthority.co.uk/media/7105/the-oga-strategy.pdf)
 1036 [strategy.pdf](https://www.nstauthority.co.uk/media/7105/the-oga-strategy.pdf)
- 1037 Ozarslan, A. (2012). Large-scale hydrogen energy storage in salt caverns. *International Journal of*
 1038 *Hydrogen Energy*, 37(19), 14265-14277. <https://doi.org/10.1016/j.ijhydene.2012.07.111>
- 1039 Peryt, T., Geluk, M., Mathiesen, M., Paul, J., & Smith, K. (2010). Chapter 8 Zechstein. In H.
 1040 Doornenbal & A. Stevenson (Eds.), *Petroleum Geological Atlas of the South Permian Basin*
 1041 *Area*.
- 1042 Pichat, A. (2022). Stratigraphy, Paleogeography and Depositional Setting of the K–Mg Salts in the
 1043 Zechstein Group of Netherlands—Implications for the Development of Salt Caverns.
 1044 *Minerals*, 12(4). <https://doi.org/10.3390/min12040486>
- 1045 Rosman, T., Bosnjak, M., Silber, H., Koßmann, J., & Heycke, T. (2022). Open science and public trust
 1046 in science: Results from two studies. *Public Understanding of Science*, 31(8), 1046-1062.
 1047 <https://doi.org/10.1177/09636625221100686>
- 1048 Samsatli, S., & Samsatli, N. J. (2019). The role of renewable hydrogen and inter-seasonal storage in
 1049 decarbonising heat – Comprehensive optimisation of future renewable energy value chains.
 1050 *Applied Energy*, 233-234, 854-893. <https://doi.org/10.1016/j.apenergy.2018.09.159>
- 1051 Sepulveda, N. A., Jenkins, J. D., Edington, A., Mallapragada, D. S., & Lester, R. K. (2021). The design
 1052 space for long-duration energy storage in decarbonized power systems. *Nature Energy*, 6(5),
 1053 506-516. <https://doi.org/10.1038/s41560-021-00796-8>
- 1054 Shan, R., Reagan, J., Castellanos, S., Kurtz, S., & Kittner, N. (2022). Evaluating emerging long-duration
 1055 energy storage technologies. *Renewable and Sustainable Energy Reviews*, 159.
 1056 <https://doi.org/10.1016/j.rser.2022.112240>
- 1057 Smdani, G., Islam, M. R., Ahmad Yahaya, A. N., & Bin Safie, S. I. (2022). Performance Evaluation of
 1058 Advanced Energy Storage Systems: A Review. *Energy & Environment*, 34(4), 1094-1141.
 1059 <https://doi.org/10.1177/0958305x221074729>
- 1060 Sobol', I. M. (2001). Global sensitivity indices for nonlinear mathematical models and their Monte
 1061 Carlo estimates. *Mathematics and Computers in Simulation*, 55(1-3), 271-280.
 1062 [https://doi.org/10.1016/s0378-4754\(00\)00270-6](https://doi.org/10.1016/s0378-4754(00)00270-6)
- 1063 Staffell, I., Green, R., Green, T., Johnson, N., & Jansen, M. (2023). *Electric Insights*. DRAX.
- 1064 Steventon, M. J., Jackson, C. A. L., Hall, M., Ireland, M. T., Munafo, M., & Roberts, K. J. (2022).
 1065 Reproducibility in Subsurface Geoscience. *Earth Science, Systems and Society*, 2.
 1066 <https://doi.org/10.3389/esss.2022.10051>
- 1067 Strozyk, F. (2017). The Internal Structure of the Zechstein Salt and Related Drilling Risks in the
 1068 Northern Netherlands. <https://doi.org/10.1016/B978-0-12-809417-4.00006-9>
- 1069 Sunny, N., Mac Dowell, N., & Shah, N. (2020). What is needed to deliver carbon-neutral heat using
 1070 hydrogen and CCS? *Energy & Environmental Science*, 13(11), 4204-4224.
 1071 <https://doi.org/10.1039/d0ee02016h>
- 1072 Svanberg, M., Ellis, J., Lundgren, J., & Landälv, I. (2018). Renewable methanol as a fuel for the
 1073 shipping industry. *Renewable and Sustainable Energy Reviews*, 94, 1217-1228.
 1074 <https://doi.org/10.1016/j.rser.2018.06.058>
- 1075 Tan, Z., Zhang, Y., Niu, J., Wenqi Ke, G. C., Zeng, H., & Liu, L. (2021). Construction Progress of Deep
 1076 Underground Salt Cavern Gas Storage and Challenges of its Drilling and Completion
 1077 Technology. *E3S Web of Conferences*, 329. <https://doi.org/10.1051/e3sconf/202132901043>
- 1078 Tarkowski, R., & Czapowski, G. (2018). Salt domes in Poland – Potential sites for hydrogen storage in
 1079 caverns. *International Journal of Hydrogen Energy*, 43(46), 21414-21427.
 1080 <https://doi.org/10.1016/j.ijhydene.2018.09.212>

1081 Teixeira, L., Lupinacci, W. M., & Maul, A. (2020). Quantitative seismic-stratigraphic interpretation of
 1082 the evaporite sequence in the Santos Basin. *Marine and Petroleum Geology*, 122.
 1083 <https://doi.org/10.1016/j.marpetgeo.2020.104690>
 1084 UK Government. (2012). *Open Data White Paper Unleashing the Potential*.
 1085 Walsh, S. D. C., Easton, L., Wang, C., & Feitz, A. J. (2023). Evaluating the Economic Potential for
 1086 Geological Hydrogen Storage in Australia. *Earth Science, Systems and Society*, 3.
 1087 <https://doi.org/10.3389/esss.2023.10074>
 1088 Warren, J. K. (2006). *Evaporites: Sediments, Resources and Hydrocarbons*. In.
 1089 <https://doi.org/10.1007/3-540-32344-9>
 1090 Williams, J. D. O., Williamson, J. P., Parkes, D., Evans, D. J., Kirk, K. L., Sunny, N., Hough, E., Vosper,
 1091 H., & Akhurst, M. C. (2022). Does the United Kingdom have sufficient geological storage
 1092 capacity to support a hydrogen economy? Estimating the salt cavern storage potential of
 1093 bedded halite formations. *Journal of Energy Storage*, 53.
 1094 <https://doi.org/10.1016/j.est.2022.105109>
 1095 Zhang, G., Liu, Y., Wang, T., Zhang, H., Wang, Z., Zhao, C., & Chen, X. (2021). Pillar stability of salt
 1096 caverns used for gas storage considering sedimentary rhythm of the interlayers. *Journal of*
 1097 *Energy Storage*, 43. <https://doi.org/10.1016/j.est.2021.103229>
 1098 Zhu, S., Shi, X., Yang, C., Li, Y., Li, H., Yang, K., Wei, X., Bai, W., & Liu, X. (2023). Hydrogen loss of salt
 1099 cavern hydrogen storage. *Renewable Energy*, 218.
 1100 <https://doi.org/10.1016/j.renene.2023.119267>

1101 **Figures**

1102 Figure. 1

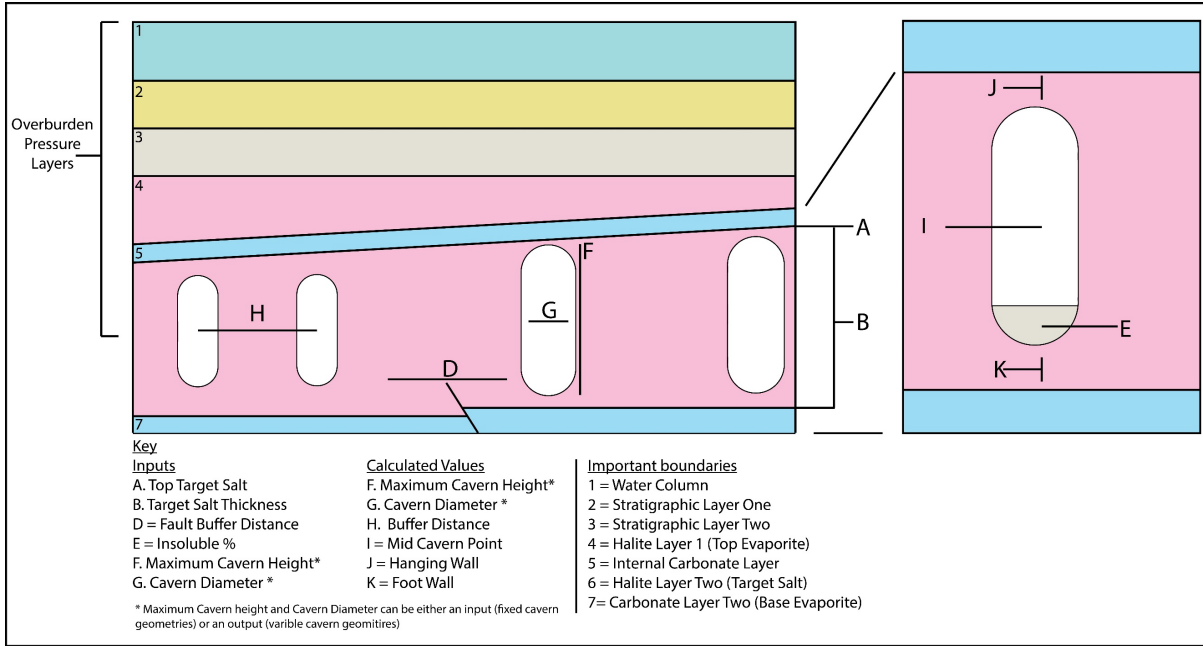


1103

1104

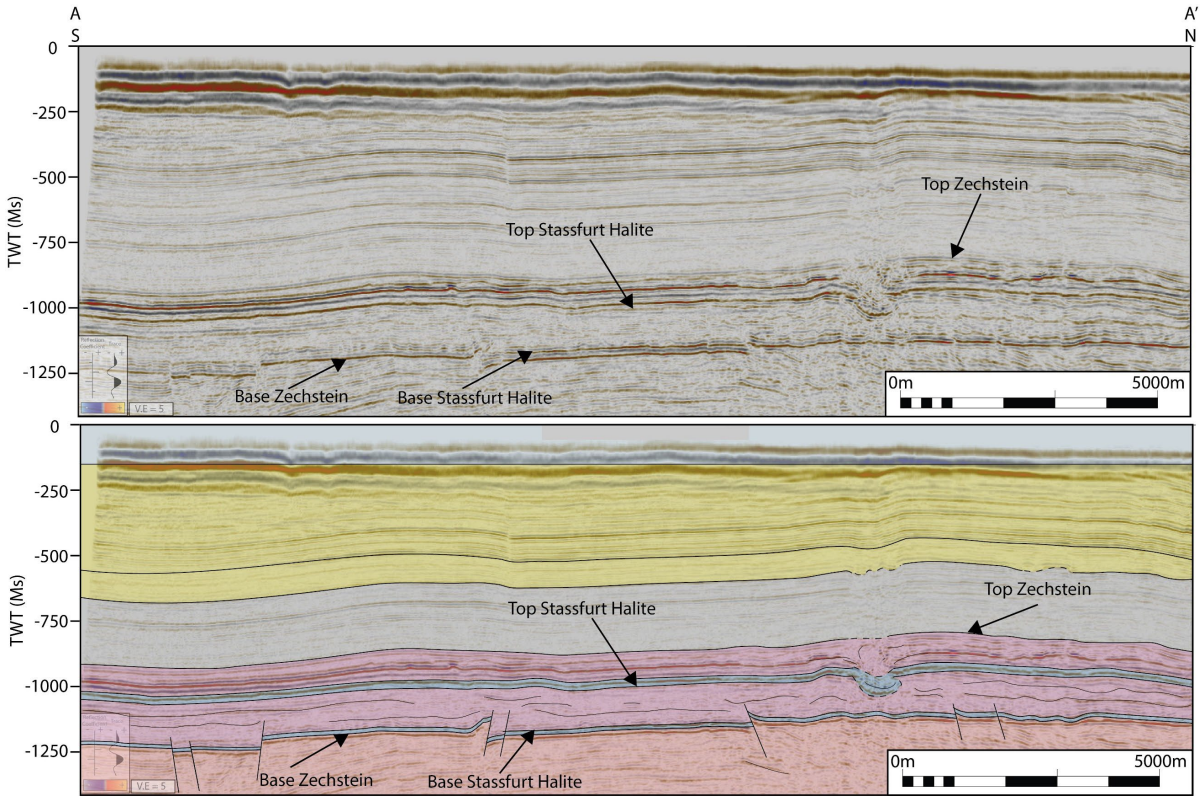
1105

1106 Figure .2



1107

1108 Figure .3



1109

1110

1111

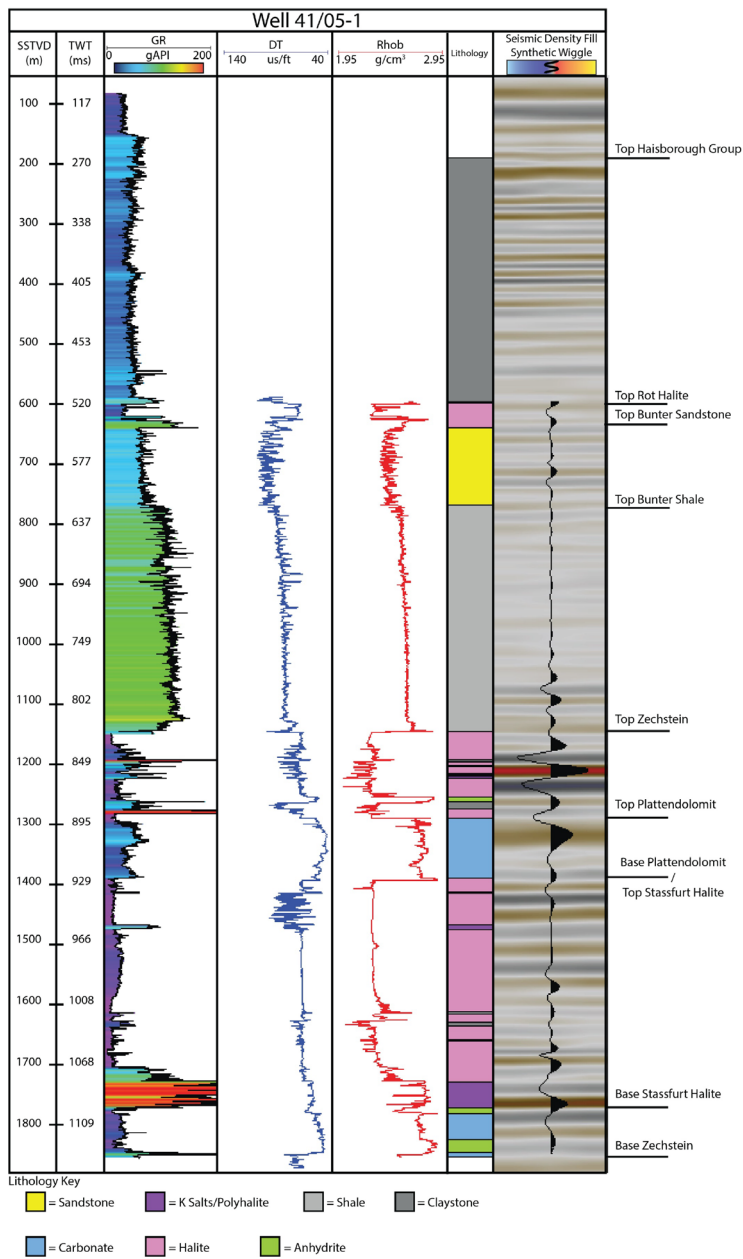
1112

1113

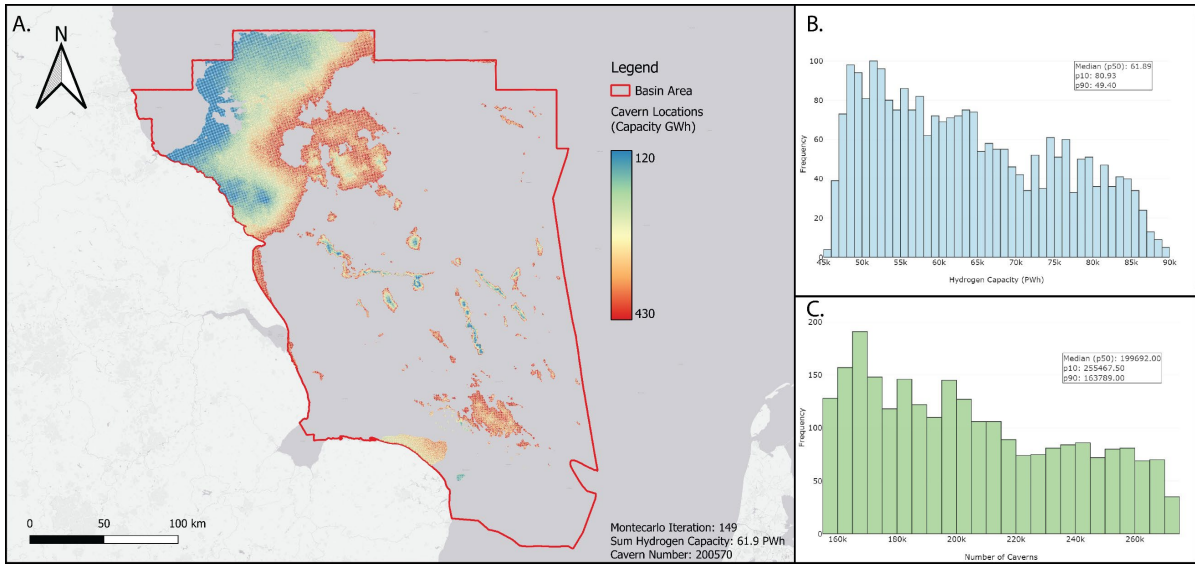
1114

1115 Figure. 4

1116

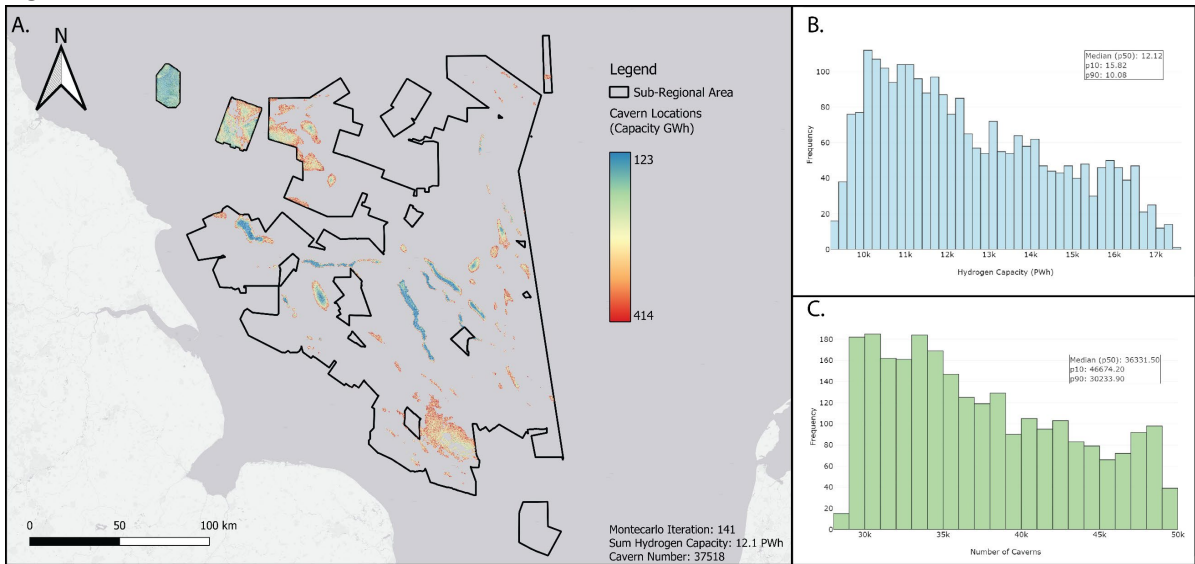


1117 Figure. 5



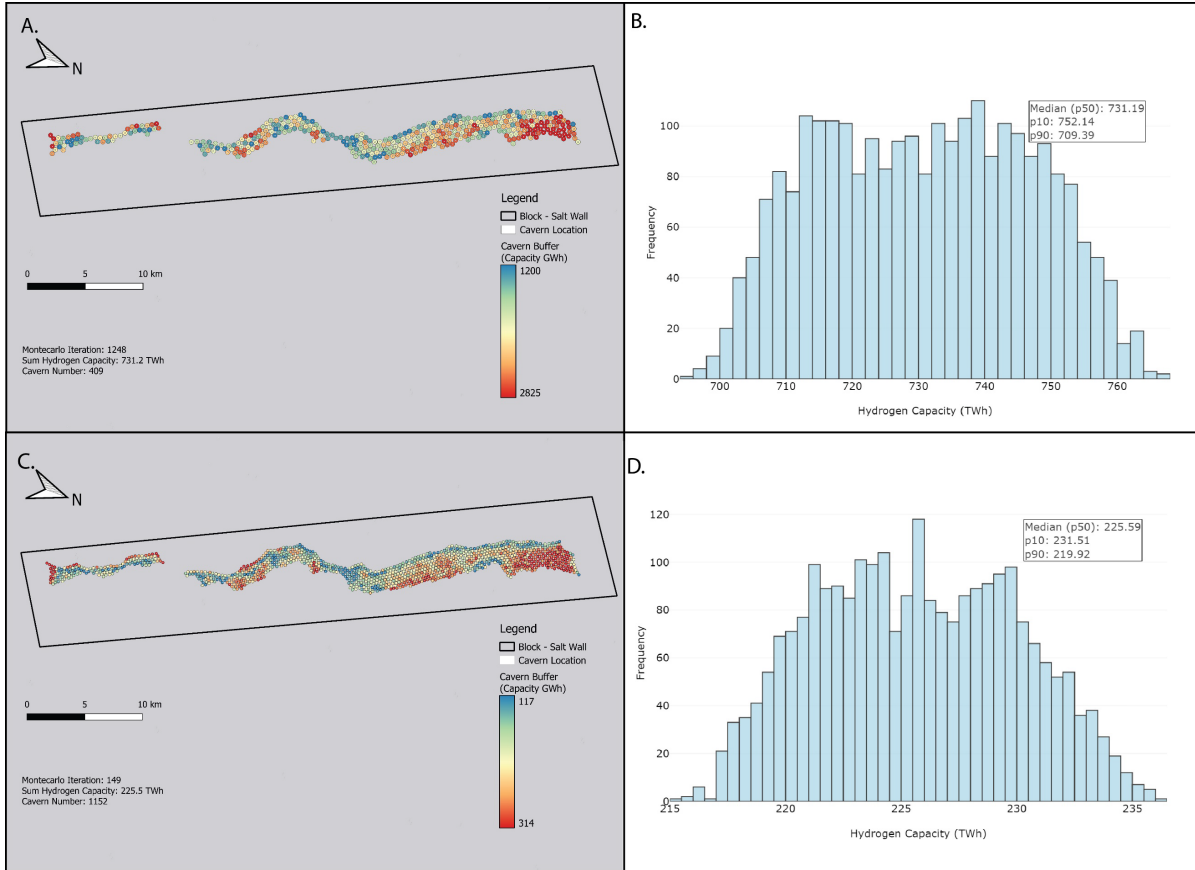
1118

1119 Figure.6



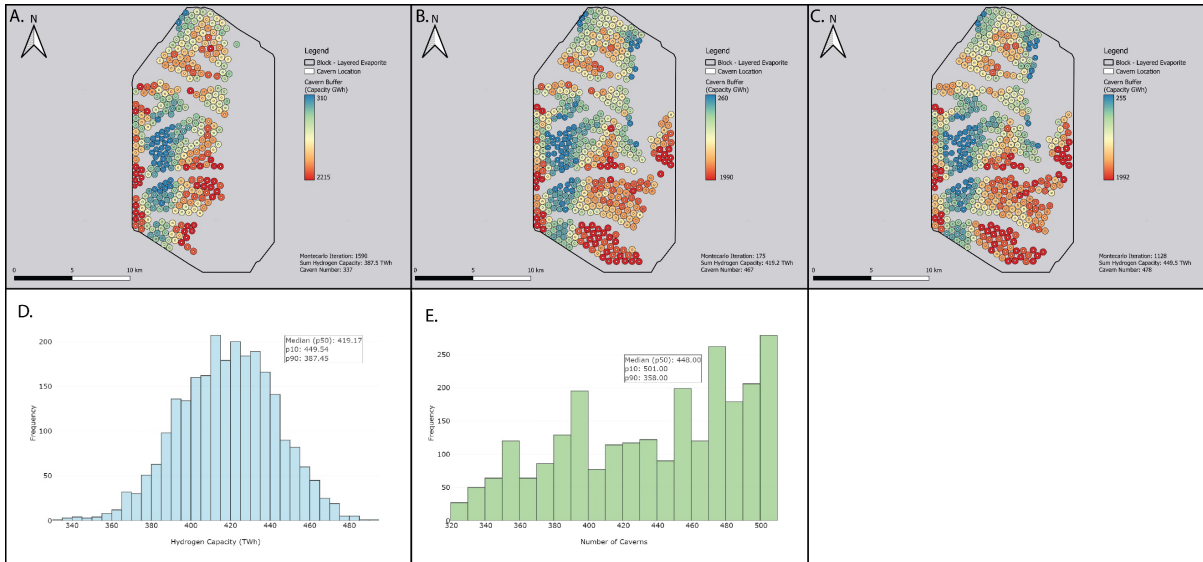
1120

1121 Figure.7



1122

1123 Figure.8



1124

1125

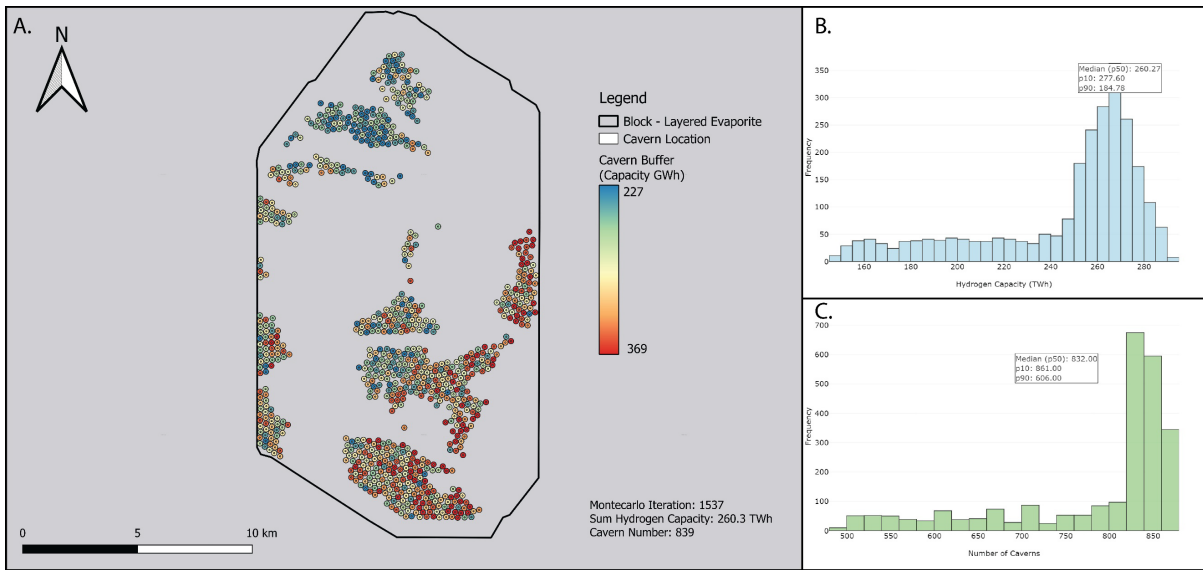
1126

1127

1128

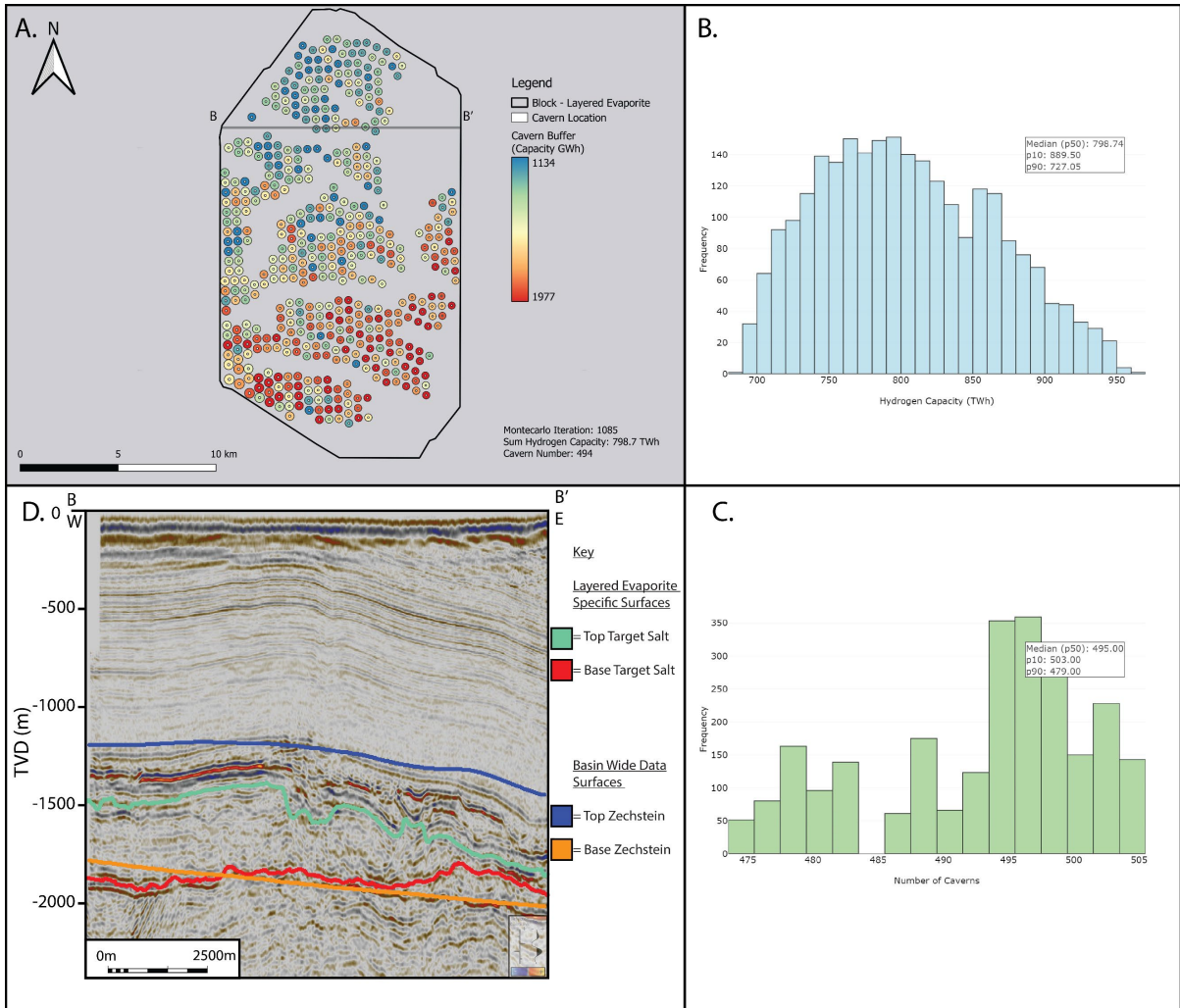
1129

1130 Figure. 9



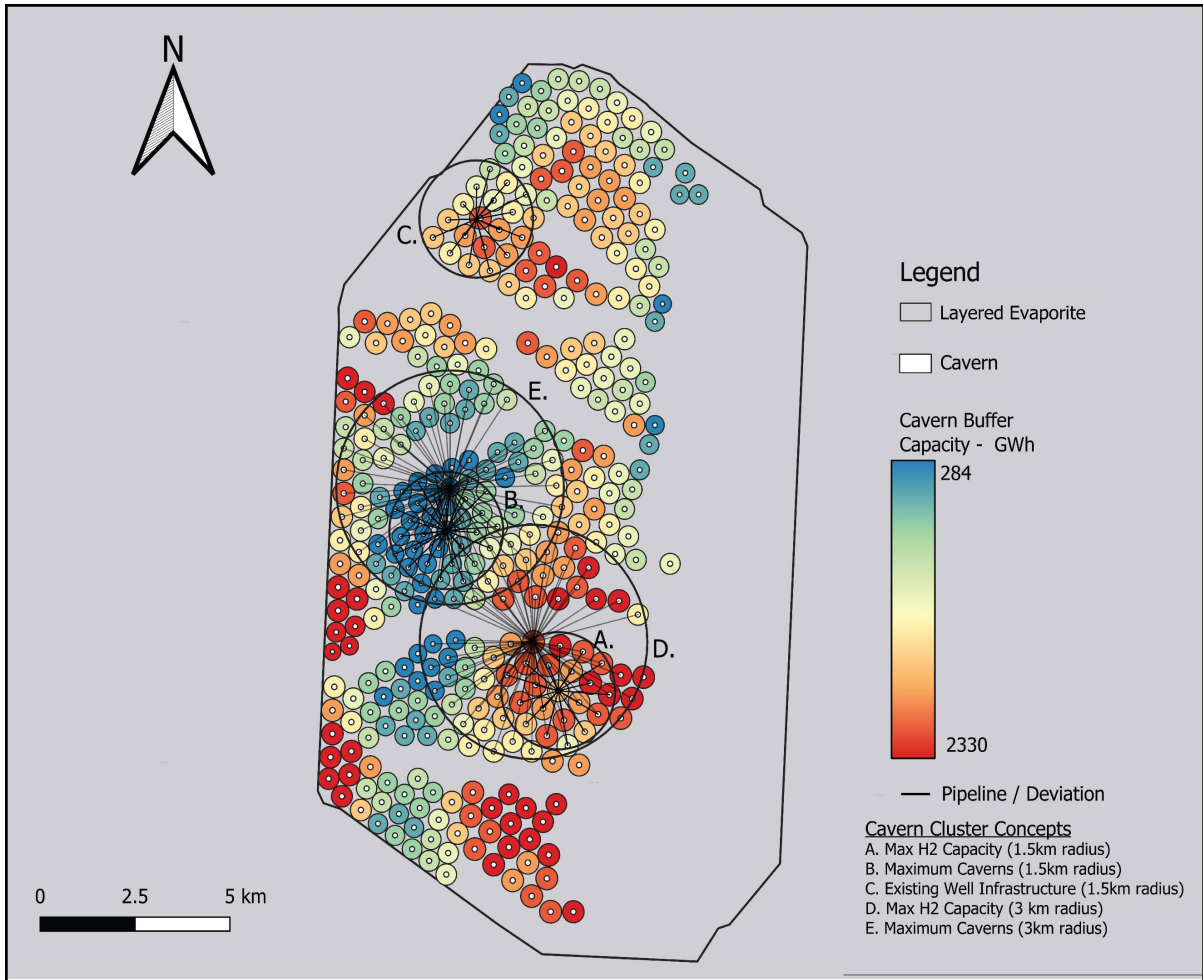
1131

1132 Figure. 10



1133

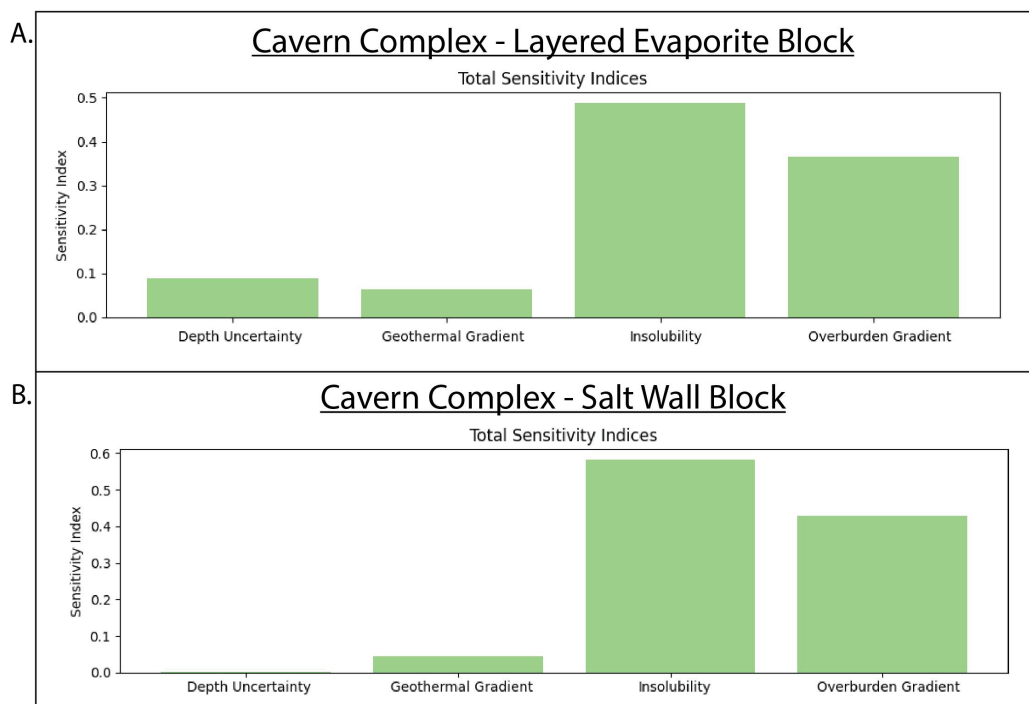
1134 Figure. 11



1135

1136

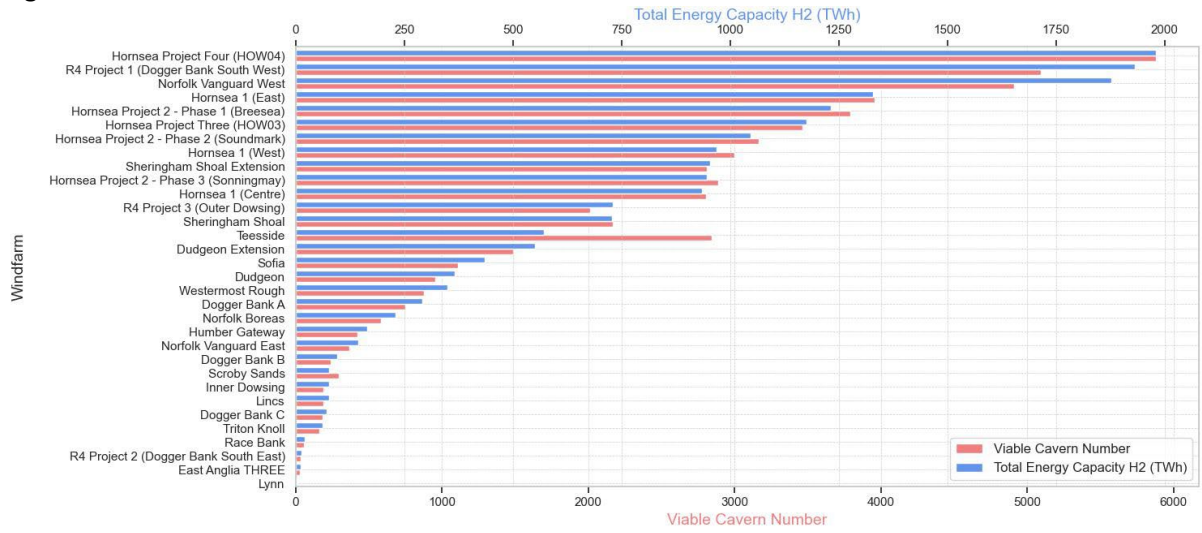
Figure. 12



1137

1138 Figure.

13



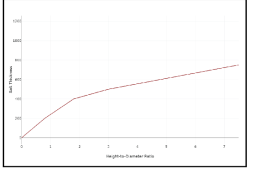
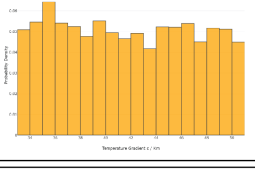
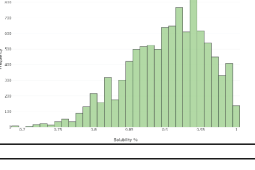
1139

1140

1141

APPENDIX FIGURES

1142 Appendix Figure 1

Workflow	Notes	Equations	Ratios / Distributions
<p>Geological Model</p> <p>↓</p> <p>Remove unviable locations</p> <p>Target Salt Depth Requirements Target Salt Thickness Requirements Faults (within buffer distance) Depositional Heterogeneities Hydrocarbon fields Other infrastructure</p> <p>↓</p> <p>Apply height-to-diameter ratio</p> <p>Dependent on specified cluster design.</p> <p>↓</p> <p>Calculate and apply cavern geometrical values</p> <p>Set on specified cavern design.</p> <p>↓</p> <p>Calculate cavern buffer size</p> <p>↓</p> <p>Calculate cavern volume</p> <p>↓</p> <p>Fit viable caverns against one another</p> <p>↓</p> <p>Apply internal lithostatic pressure values to caverns</p> <p>↓</p> <p>Apply internal temperature to caverns</p> <p>↓</p> <p>Apply insoluble content % to caverns</p> <p>↓</p> <p>Calculate H₂ capacity for caverns</p> <p>↓</p> <p>Sum H₂ capacity for caverns in AOI</p> <p>OR</p> <p>Sum H₂ capacity for caverns in cluster concept</p> <p>Cluster concept can be chosen as seen fit to develop within the area of interest</p>	<p>Remove unviable locations</p> <p>Removes areas that are designated as being unsuitable for the emplacement of salt caverns. Can be modified as such to include other parameters. Eg if onshore, roads or other infrastructure</p> <p>Apply height-to-diameter ratio</p> <p>Can be ignored if static cavern design is used. If viable caverns are chosen, a set constant can be used. Constant can be set or interpolated from a table.</p> <p>Calculate Cavern Volume</p> <p>Cavern geometrical 3D shape can be chosen dependent upon requirements. Typically pill or ellipsoid geometries are chosen.</p> <p>Fit viable caverns against one another</p> <p>Higher resolution grids for geological surfaces allows for better packing within viable area</p> <p>Apply internal lithostatic pressure values to caverns</p> <p>Depending on geological model, calculation can be simple (1D) or complex (3D)</p> <p>Apply internal temperature to caverns</p> <p>Depending on geological model, can be simple (geothermal gradient of area) or complex (heat flow model of area)</p> <p>Calculate H₂ capacity for caverns</p> <p>Can be modified for different energy vectors. Eg Ammonia or Natural Gas</p>	<p>Calculate and apply cavern geometrical values</p> <p>Equation 2: Max cavern height = available salt thickness / (1 + 0.95 / height to diameter ratio) Equation 3: Cavern diameter = Max cavern height / height to diameter ratio Equation 4: Cavern hanging wall = 0.2 * cavern diameter Equation 5: Cavern footwall = 0.75 * cavern diameter Equation 6: Mid cavern depth = Salt depth + hanging wall thickness + (max cavern height/2)</p> <p>Calculate cavern buffer size</p> <p>Equation 7: Cavern buffer (from cavern midpoint) = 2 * Cavern diameter</p> <p>Calculate cavern volume</p> <p>Equation 8: Cavern volume (pill) = $\pi r^2(H - 2r) + (4/3)\pi r^3$ Equation 8b: Cavern volume (ellipsoid) = $4/3 * \pi r^3(H/2)$</p> <p>Calculate cavern lithostatic pressure</p> <p>Equation 9: Layer Lithostatic Pressure (Figure X) Lithostatic pressure (MPa) = $\sum L1(\rho^*g*62) + L2(\rho^*g*62) + L3(\rho^*g*62)...$ Note* Lithostatic pressure calculated for major change in geological interval L1 - Layer 1, L2 = Layer 2... Equation 9b: Simple 1D Lithostatic Lithostatic pressure (MPa) = (Lithostatic pressure gradient * (Cavern midpoint Z - Seabed Z)) + (Water pressure gradient * (Seabed Z - Datum))</p> <p>Calculate cavern internal temperature</p> <p>Equation 10: Cavern temperature = Sea bed temperature + (Cavern midpoint (z) * Geothermal gradient)</p> <p>Calculate cavern volume (including insolubles)</p> <p>Equation 11: Cavern volume actual = Cavern volume * Insoluble content</p> <p>Calculate cavern energy capacity</p> <p>Equation 12: $E = ((P^{0.6}) * V / R * T) * 2.016 * 10^3 * 142 * 2.78 * 10^7$ E = Energy (GWh) P = Internal cavern pressure (MPa). V = Cavern volume (M³) T = Temperature (K) 2.016 * 10³ = Molar mass of H₂ 142 MJ/KG = Lower heating value of H₂ 2.78 * 10⁷ = Conversion from MJ to GWh</p> <p>Calculate cavern/cluster energy capacity</p> <p>Equation 13: Total AOI H₂ capacity = $\sum H_2$ capacity caverns Equation 13b: Total Cluster H₂ capacity = $\sum H_2$ capacity caverns in cluster concept area</p>	<p>Height-to-diameter ratio interpolation table</p>  <p>Geothermal gradient c/km distribution</p>  <p>Solubility distribution</p> 

1143

1144

1145

1146

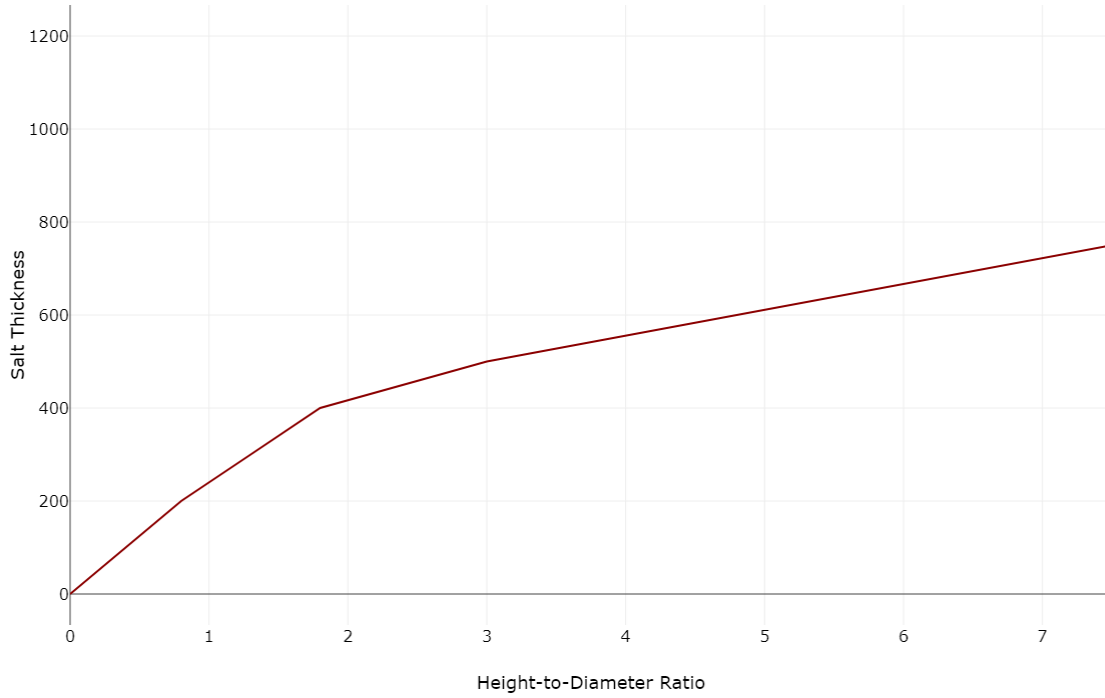
1147

1148

1149

1150 Appendix Figure 2

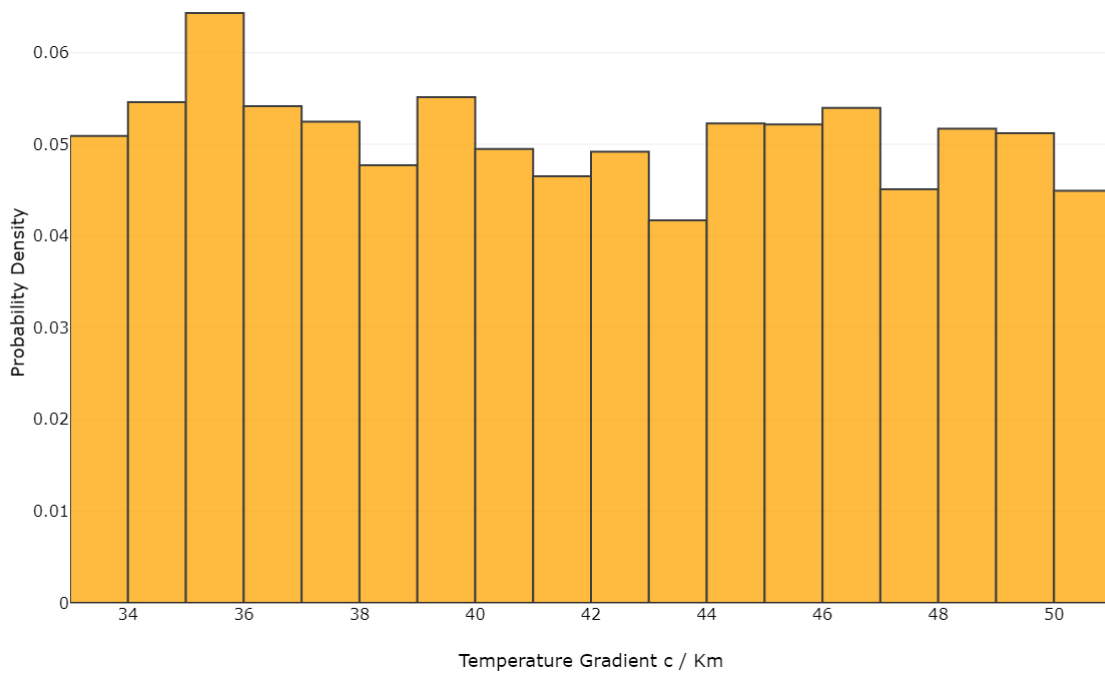
1151



1152

1153 Appendix Figure 3

1154 A

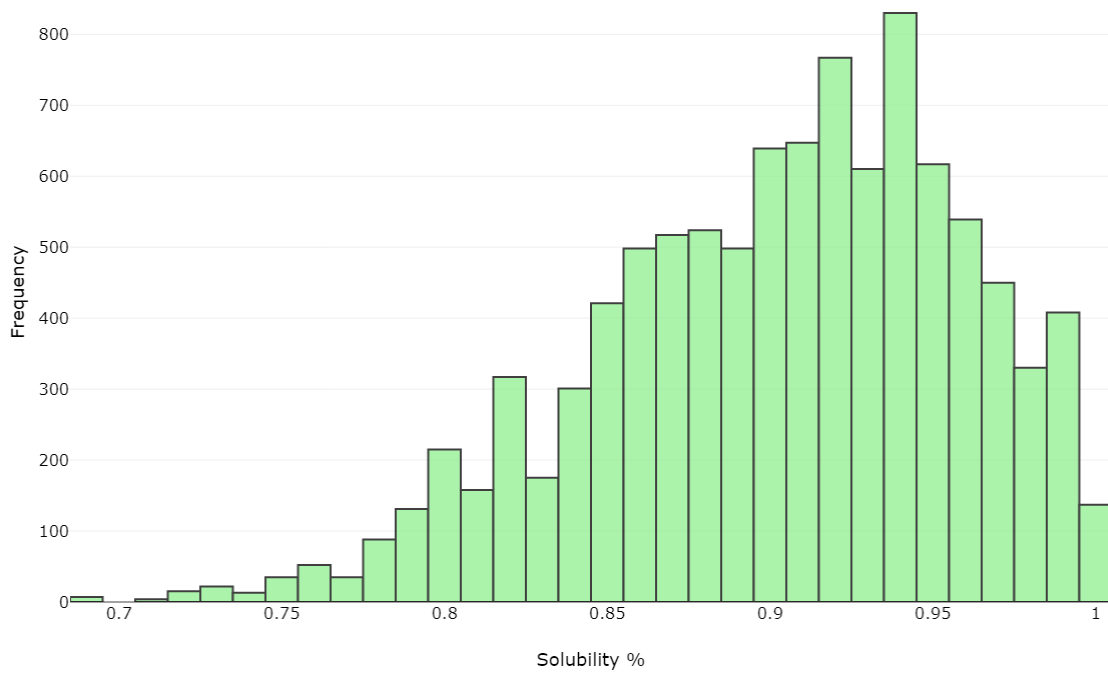


1155

1156

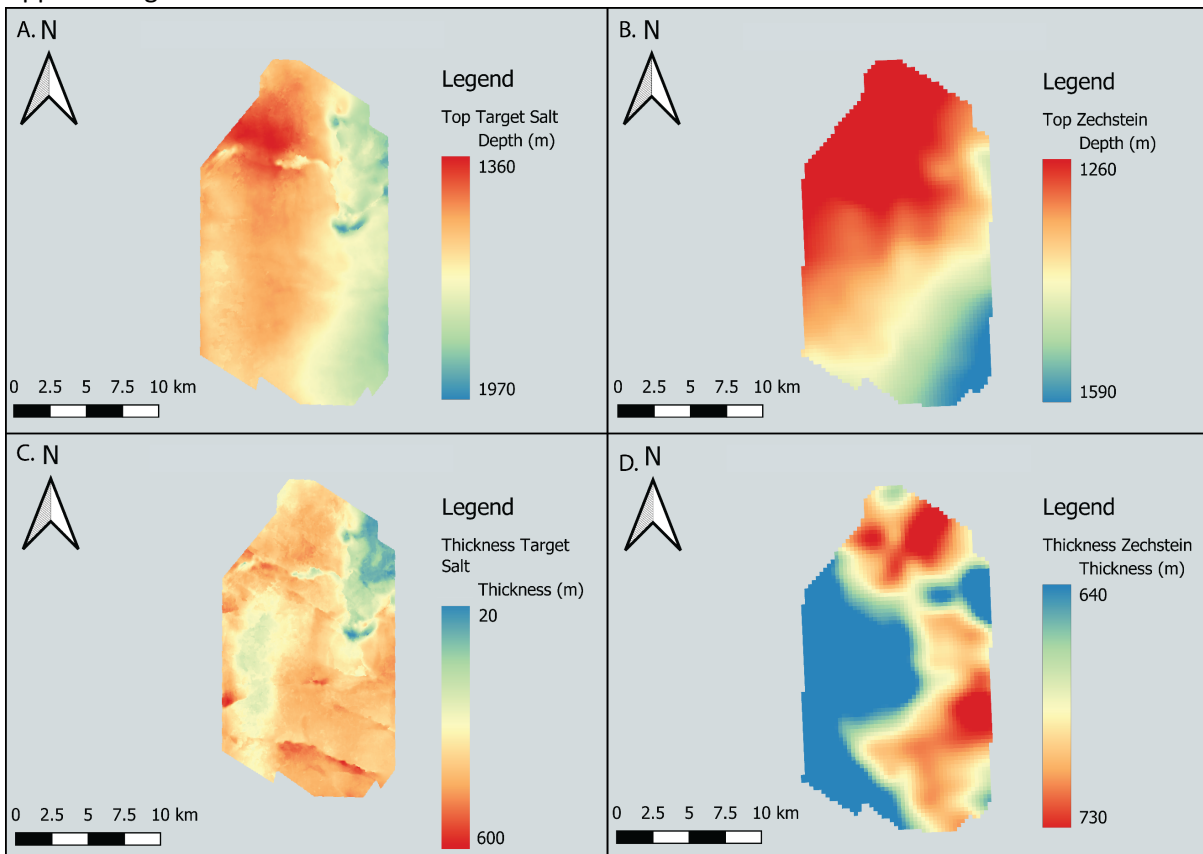
1157

1158 Appendix Figure 4



1159

1160 Appendix Figure 5

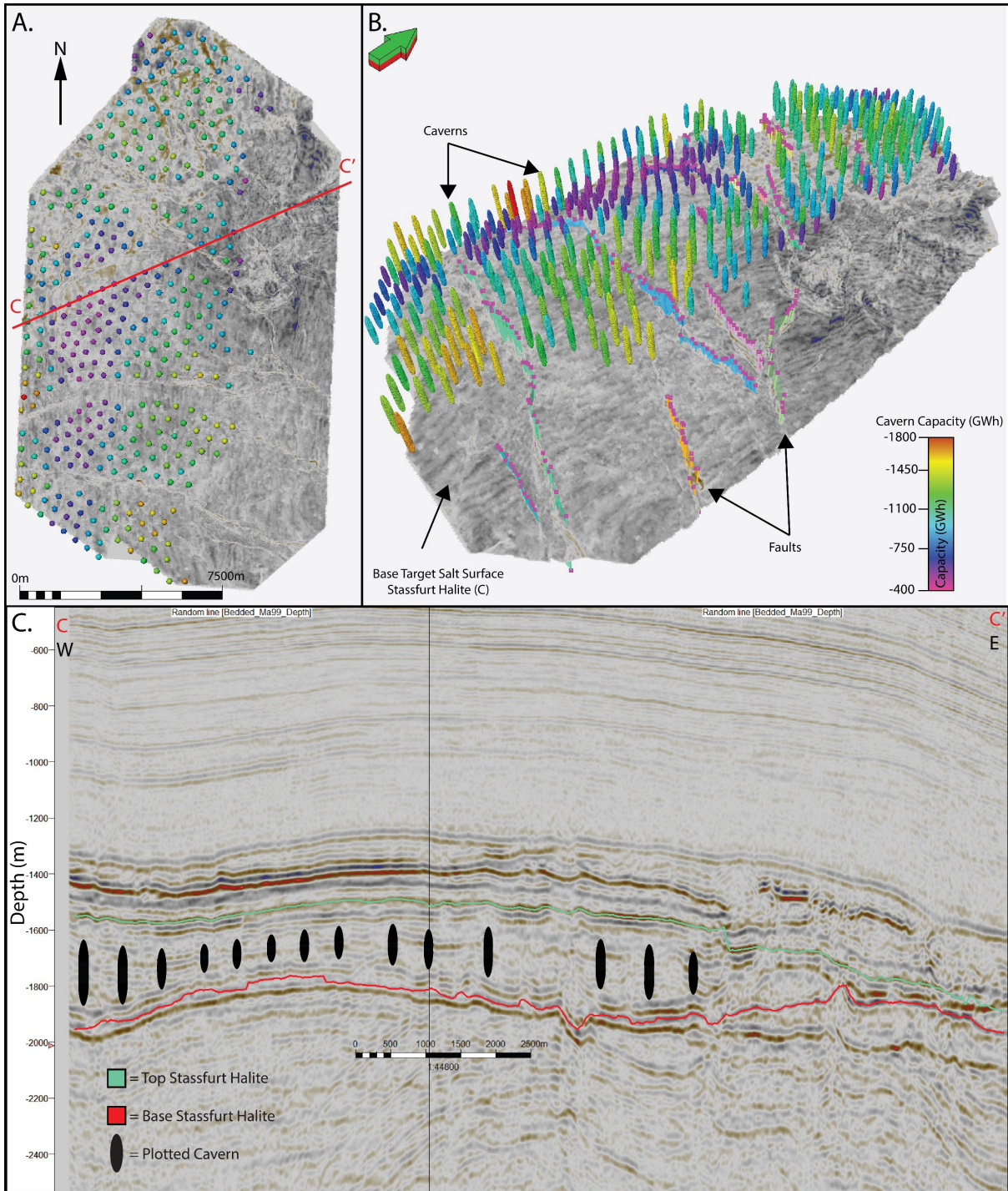


1161

1162

1163

1164



1166

1167

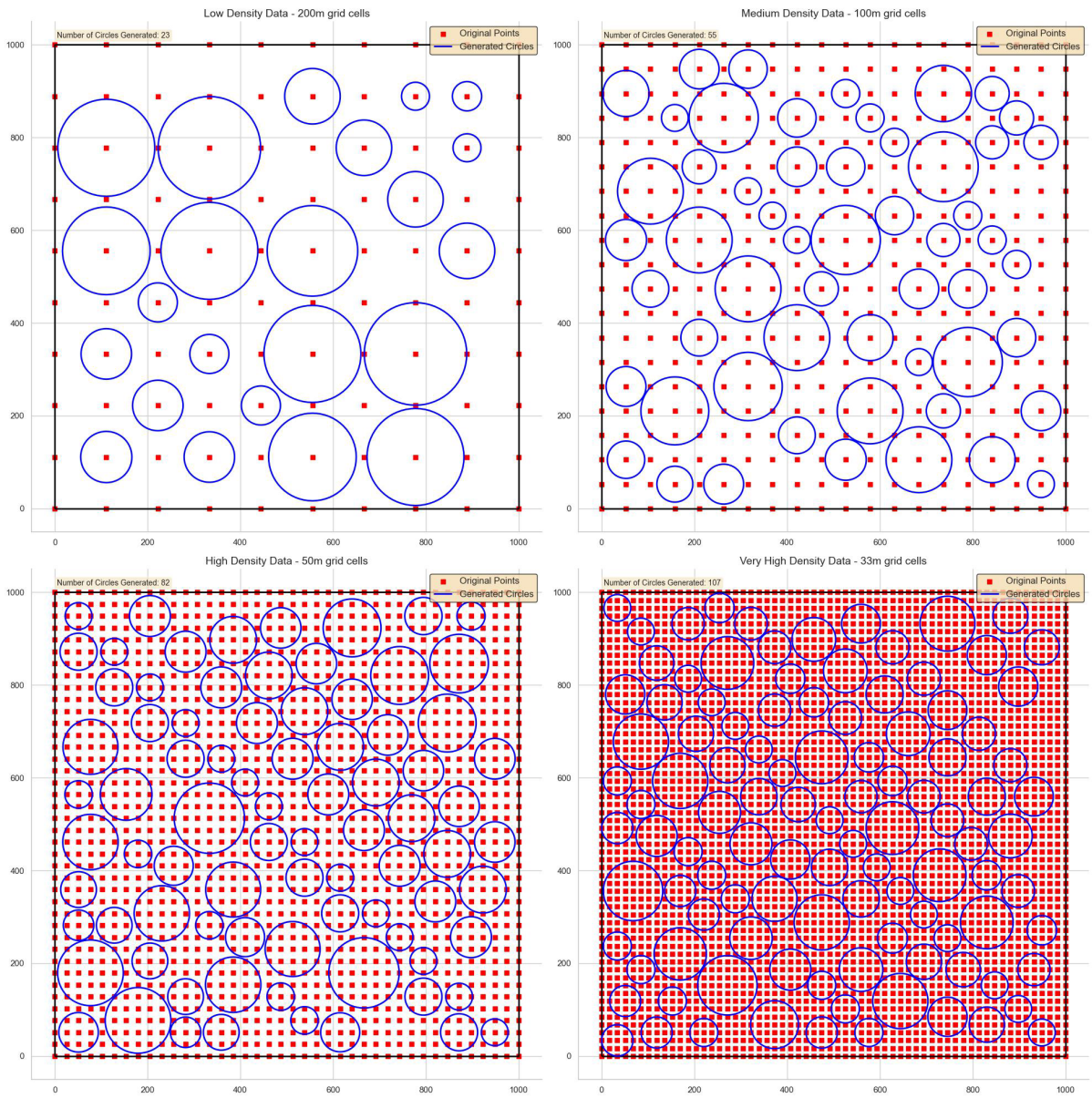
1168

1169

1170

1171

1172



Appendix Figure Captions

Appendix 1 - Workflow, equations, and ratios/distribution used for the workflow described in Section. 2. 1

Appendix 2 – Height-to-diameter ratio pre-set relationship.

Appendix 3 – Geothermal gradient C / Km uniform distribution from the Southern North Sea used within workflow.

Appendix 4 – Zechstein Stassfurt halite solubility % distribution within the Southern North Sea

Appendix 5 - Data comparisons between surfaces from 'Block – Layered Evaporite' Aol specific geological models (Section 4.4.1-2) basin wide depth surfaces (Section 4.4.3). A and B are depth surfaces, A is for the Top target salt the top Stassfurt halite (Figure. 5), interpreted from seismic data specifically for this study (Used in sections 4.4.1-2), while B is the top Zechstein from the Basin Wide geological model cut to the layered evaporite area (Section 4.4.3), cross sections on seismic data of both surfaces can be seen in Figure. 11. C and D are thickness surfaces, C was calculated from top and base Stassfurt halite interpreted from seismic data, D is the thickness of top and base Zechstein from the Basin Wide geological model.

Appendix 6 – Salt caverns within in 3D and 2D space plotted against seismic data (TVD). The salt caverns plotted are the 'Block - Layered Evaporite' Aol with variable caverns (Section 4.4.1). A) Shows caverns coloured for total hydrogen capacity, with the base Stassfurt halite seismic horizon probe surface. B) Shows the same as A, however the camera has been rotated to an angled view, and faults have been displayed on the 3D image, as sticks topped with pink dots. C) A 2d seismic cross-section in TVD (m), C – C' (Appendix 3, A), running west to east. Top and base Stassfurt halite reflections have been marked on in green and red respectively. Caverns have been plotted in their correct locations. Note how caverns avoid faults.

Appendix 7 – Synthetic grid data surfaces of varying data density (200 m – 33 m) with circles generated using the same buffer packing function that is used within the cavern placement workflow (Section. 2.1). The different grid densities and generated circles demonstrate how input grid density (geological model grid cell density) affects the location and placement of caverns.

Appendix - Further Info - Best fit algorithm

The best fit algorithm initiates with the list of all viable cavern locations calculated previously in the workflow. Each viable grid cell has an associated cavern and cavern data. The algorithm iterates down the list of viable cavern locations (The spatial order being top left to top right then continuing from the row below again from left to right, finishing in the bottom right of the grid). From the viable caverns, it generates a polygon of equal radius to the required buffer radius depending on the size of the cavern. The buffer polygon is then plotted within the viable area polygon, and checks are made to see if it overlaps with another buffer polygon, if it does overlap, it is removed from the table of viable caverns and the algorithm continues onto the next cavern in the list. The algorithm iterates through every viable cavern location, discarding those that overlap with other caverns. The final product is caverns best fitting within the AOI.

43 **Appendix - Further Info Depth Uncertainty**

44 Depth conversion and uncertainty used the methodology laid out in (Barnett et al., 2023)

45 **Appendix – Tables**

46

47 Appendix Table A – Key stratigraphic surfaces used for the layered evaporite geological model.

48

49

Geological Horizon - Mapped
Seabed
Base Bunter Sandstone
Top Zechstein (Base bunter Shale)
Top Stassfurt Halite
Base Stassfurt Halite (above basal polyhalite reflection)
Base Zechstein

50

51

52

53

54

55

56 Table B: Geological models run through proposed workflow with identified geological
57 parametrisations.

58

Model/Study	Max Salt Depth (Top Cavern) (m)	Minimum Salt Depth (Top Cavern) (m)	Min Salt thickness (m)	Top Salt Surface	Base Salt Surface	Depth Model	Grid Cell Resolution (m)	Temperature (c)	Overburden Pressure Model	Insoluble Content (%)	Cavern Geometry	Depth Uncertainty (%)	Exclusion Zones	Total Area Km ²
Basin Wide – Fixed Caverns	1700	500	358.5	Top Zechstein (Stochastic)	Base Zechstein (Stochastic)	Basin Wide Salt Depth Model (Section 3.1)	250	Distribution, see Appendix (Stochastic)	Gradient – 0.02354 MPa/m (2400kg/m3 equivalent) (Deterministic)	Distribution, see Appendix (Stochastic)	Height: 300 Diameter: 58	10	None	58,904
Sub-Regional - Fixed Caverns	1700	500	358.5	Top Zechstein (Stochastic)	Base Zechstein (Stochastic)	Sub Regional Salt Depth Model (Section 3.2)	50	Distribution, see Appendix (Stochastic)	Gradient – 0.02354 MPa/m (2400kg/m3 equivalent) (Deterministic, but linked to depth uncertainty)	Distribution, see Appendix (Stochastic)	Height: 300 Diameter: 58	5	None	25,000
Layered Evaporite – Variable Caverns	1700	500	200	Top Stassfurt Halite (Stochastic)	Base Stassfurt Halite (Stochastic)	Layered Evaporite Salt Depth Model (Section 3.3.2)	50	Distribution, see Appendix (Stochastic)	Layer cake model (Stochastic)	Distribution, see Appendix (Stochastic)	Variable, Set from height-to-diameter ratio, See Appendix . Maximum height 750 m	7	Interpreted heterogeneity in seismic, Faults (250 m buffer)	238.5
Layered Evaporite – Fixed Caverns	1700	500	358.5	Top Stassfurt Halite (Stochastic)	Base Stassfurt Halite (Stochastic)	Layered Evaporite Salt Depth Model (Section 3.3.2)	50	Distribution, see Appendix (Stochastic)	Layer cake model (Stochastic)	Distribution, see Appendix (Stochastic)	Height: 300 Diameter: 58	7	Interpreted heterogeneity in seismic, Faults (250 m buffer)	238.5
Layered Evaporite - Basin Wide Data - Variable Caverns	1700	500	200	Top Zechstein (Stochastic)	Base Zechstein (Stochastic)	Layered Evaporite Salt Depth Model (Section 3.3.2)	50	Distribution, see Appendix (Stochastic)	Layer cake model (Stochastic)	Distribution, see Appendix (Stochastic)	Variable, Set from height-to-diameter ratio, See Appendix. Maximum height 750 m	10	Interpreted heterogeneity in seismic, Faults (250 m buffer)	238.5

Salt Wall – Variable Caverns	1700	500	200	Top Zechstein (Stochastic)	Base Zechstein (Stochastic)	Sub Regional Salt Depth Model (Section 3.2, cut for Salt – Wall Block)	50	Distribution, see Appendix (Stochastic)	Gradient – 0.2305 MPa/m (2040kg/m ³ equivalent) (Deterministic, but linked to depth uncertainty)	Distribution, see Appendix (Stochastic)	Variable, Set from height-to-diameter ratio, See Appendix. Maximum height 750 m	5	500m buffer away from salt wall edges	420
Salt Wall – Fixed Caverns	1700	500	358.5	Top Zechstein (Stochastic)	Base Zechstein (Stochastic)	Sub Regional Salt Depth Model (Section 3.2, cut for Salt – Wall - Block)	50	Distribution, see Appendix (Stochastic)	Gradient – 0.2305 MPa/m (2040kg/m ³ equivalent) (Deterministic, but linked to depth uncertainty)	Distribution, see Appendix (Stochastic)	Height: 300 Diameter: 58	5	500m buffer away from salt wall edges	420

59

60

Table C. – Salt cavern parameters within workflow.

61

Parameter	Value
Depth to target salt	500 – 2000 m (Caglayan et al., 2020; Tan et al., 2021; Warren, 2006)
Target salt thickness	>200m (Caglayan et al., 2020; Smith et al., 2005; Wang et al., 2015).
Structural heterogeneities	Mapped parameter, buffer set at 250m (Chen et al., 2022; Yang et al., 2013)
Height – to – diameter ratio	0.5 minimum (Caglayan et al., 2020; Wang et al., 2015) Typical no greater than 7.5
Fixed Cavern Size	300 m tall 58.5 m Diameter
Variable Cavern Size	Maximum Cavern Height: 750 m Minimum cavern height: 91.5 m (based on minimum salt thickness 200 m) Maximum height-to-diameter ratio: 7.5 Minimum height-to-diameter ratio: 0.8
Target salt Solubility	No value requirements, needed for hydrogen capacity calculation. Ideally as high as possible.
Energy system integration	Mapped parameter

62

63 Table D: Inputs for Sobol sensitivity analysis on layered evaporite block and salt wall block.

64

Variable	Value(s)	Distribution type
Depth uncertainty (%)	+ - 5	Uniform

Geothermal Gradient (°c)	32 – 52	Uniform
Insoluble Content (%)	Mean - 92 Standard Deviation - 7.2 Truncation - 64 - 1	Truncated Normal
Overburden Pressure Gradient MPa/m	0.021 - 0.025	Uniform

65

66 Table E. Comparison of results to other studies. *Note results from this study regarding cavern
67 number are obtained from the Montecarlo iteration (Iteration number in brackets, see data
68 for Montecarlo iteration list) with the closest total hydrogen capacity to the calculated p50
69 for that model run. * = models from this study.

70

Study	Basin/Area	Working Hydrogen Capacity (TWh)	Number of Caverns	Average Cavern Working Capacity (GWh)	Cavern dimensions
Williams et al. (2022)	Cheshire Basin	129	1297	99.4	Height: 20 -262 Diameter: 100 m
Williams et al. (2022)	Wessex Basin	557	3378	164.8	Height: Variable Diameter: 100 m
Williams et al. (2022)	East Yorkshire	1465	8425	173.9	Height: Variable Diameter: 100 m
The Royal Society (2023)	East Yorkshire	≈100	3000	33.3 (Estimates of 120 in chosen locations)	Height 100m Diameter 31m Raw Volume: 300,000
Caglayan et al. (2020)	Offshore UK (Southern North Sea, Salt structures only)	9,000	NA	NA	Height 300 Diameter 58 Raw Volume: 750,000
*Basin Wide – Fixed Caverns – p50 (Iteration: 149)	Offshore UK (Southern North Sea, 58,904 km ²)	61,885	200,570	308.5	Height 300 Diameter 58 Raw Volume: 750,000
Allsop et al. (2023)	Offshore UK – (Mega Merge Area - Southern North Sea)	53 - 292	1485	35.6 / 196.6	Height 300 Diameter 58 Raw Volume 750,000
*Sub-Regional – Fixed Caverns – p50 (Iteration: 141)	Offshore UK – (Mega Merge Area – Southern North Sea, 25,000 km ²)	12,124	37,518	323	Height 300 Diameter 58 Raw Volume: 750,000
Allsop et al. (2023)	Audrey Salt Wall	23 - 105	105	219 / 1005	Height 300 Diameter 58 Raw Volume: 750,000
*Salt Wall - Fixed Caverns - p50 (Iteration: 149)	Audrey Salt Wall	225	1152	195	Height 300 Diameter 58 Raw Volume: 750,000
*Salt Wall – Variable Caverns - p50 (Iteration: 1248)	Audrey Salt Wall	731	409	1787	Variable
*Layered Evaporite - Variable Caverns - p50 (Iteration: 175)	Seismic Survey - MA933F002	419	467	897	Variable
*Layered Evaporite – Basin Wide Depth Model Data - Variable Caverns p50 (Iteration: 1085)	Seismic Survey - MA933F002	799	494	1617	Variable
*Layered Evaporite – Fixed Caverns p50 (Iteration: 1537)	Seismic Survey - MA933F002	260	839	309	Height 300 Diameter 58 Raw Volume: 750,000

71

72

73 **Bibliography Supplementary Materials**

74

75 Allsop, C., Yfantis, G., Passaris, E., & Edlmann, K. (2023). Utilizing publicly available datasets for
76 identifying offshore salt strata and developing salt caverns for hydrogen storage. *Geological*
77 *Society, London, Special Publications*, 528(1), 139-169. [https://doi.org/10.1144/sp528-2022-](https://doi.org/10.1144/sp528-2022-82)
78 [82](https://doi.org/10.1144/sp528-2022-82)

79 Barnett, H. G., Ireland, M. T., & van der Land, C. (2023). Characterising the internal structural
80 complexity of the Southern North Sea Zechstein Supergroup Evaporites. *Basin Research*, 35(5),
81 1651-1673. <https://doi.org/10.1111/bre.12768>

82 Caglayan, D. G., Weber, N., Heinrichs, H. U., Linßen, J., Robinius, M., Kukla, P. A., & Stolten, D. (2020).
83 Technical potential of salt caverns for hydrogen storage in Europe. *International Journal of*
84 *Hydrogen Energy*, 45(11), 6793-6805. <https://doi.org/10.1016/j.ijhydene.2019.12.161>

85 Chen, X.-S., Li, Y.-P., Jiang, Y.-L., Liu, Y.-X., & Zhang, T. (2022). Theoretical research on gas seepage in
86 the formations surrounding bedded gas storage salt cavern. *Petroleum Science*, 19(4), 1766-
87 1778. <https://doi.org/10.1016/j.petsci.2022.01.021>

88 Smith, N. J. P., Evans, D. J., & Andrews, I. J. (2005). *The Geology of Gas Storage in Offshore Salt Caverns*.
89 https://itportal.ogauthority.co.uk/information/papers/BGS_Report1.pdf

90 Tan, Z., Zhang, Y., Niu, J., Wenqi Ke, G. C., Zeng, H., & Liu, L. (2021). Construction Progress of Deep
91 Underground Salt Cavern Gas Storage and Challenges of its Drilling and Completion
92 Technology. *E3S Web of Conferences*, 329. <https://doi.org/10.1051/e3sconf/202132901043>

93 The Royal Society. (2023). *Large-scale electricity storage policy briefing* (978-1-78252-666-7).

94 Wang, T., Yang, C., Ma, H., Daemen, J. J. K., & Wu, H. (2015). Safety evaluation of gas storage caverns
95 located close to a tectonic fault. *Journal of Natural Gas Science and Engineering*, 23, 281-293.
96 <https://doi.org/10.1016/j.jngse.2015.02.005>

97 Warren, J. K. (2006). Evaporites: Sediments, Resources and Hydrocarbons. In.
98 <https://doi.org/10.1007/3-540-32344-9>

99 Williams, J. D. O., Williamson, J. P., Parkes, D., Evans, D. J., Kirk, K. L., Sunny, N., Hough, E., Vosper, H.,
100 & Akhurst, M. C. (2022). Does the United Kingdom have sufficient geological storage capacity
101 to support a hydrogen economy? Estimating the salt cavern storage potential of bedded halite
102 formations. *Journal of Energy Storage*, 53. <https://doi.org/10.1016/j.est.2022.105109>

103 Yang, C., Jing, W., Daemen, J. J. K., Zhang, G., & Du, C. (2013). Analysis of major risks associated with
104 hydrocarbon storage caverns in bedded salt rock. *Reliability Engineering & System Safety*, 113,
105 94-111. <https://doi.org/10.1016/j.ress.2012.12.017>

106